Monthly Notices
of the
ROYAL ASTRONOMICAL SOCIETY

MNRAS **436,** 2793–2809 (2013)
Advance Access publication 2013 October 15

doi:10.1093/mnras/stt1775

^{13}CO and C^{18}O emission from a dense gas disc at $z = 2.3$: abundance variations, cosmic rays and the initial conditions for star formation

A. L. R. Danielson,[1]⋆ A. M. Swinbank,[1] Ian Smail,[1] E. Bayet,[2] Paul P. van der Werf,[3] P. Cox,[4] A. C. Edge,[1] C. Henkel[5,6] and R. J. Ivison[7,8]

[1]*Institute for Computational Cosmology, Department of Physics, Durham University, South Road, Durham DH1 3LE, UK*
[2]*Sub-Department of Astrophysics, University of Oxford, Denys Wilkinson Building, Keble Road, Oxford OX1 3RH, UK*
[3]*Leiden Observatory, Leiden University, PO Box 9513, NL-2300 RA Leiden, the Netherlands*
[4]*Institut de Radio Astronomie Millimetrique, 300 rue de la Piscine, Domaine Universitaire, F-38406 Saint Martin d'Heres, France*
[5]*Max-Planck-Institut fur Radioastronomie, Auf dem Hugel 69, D-53121, Bonn, Germany*
[6]*Department of Astronomy, King Abdulaziz University, PO Box 80203, Jeddah, Saudi Arabia*
[7]*UK Astronomy Technology Centre, Royal Observatory, Blackford Hill, Edinburgh EH9 3HJ, UK*
[8]*Institute for Astronomy, University of Edinburgh, Edinburgh EH9 3HJ, UK*

Accepted 2013 September 19. Received 2013 August 29; in original form 2012 December 21

ABSTRACT

We analyse the spectral line energy distributions of ^{13}CO and C^{18}O for the $J = 1\rightarrow0$ up to $J = 7\rightarrow6$ transitions in the gravitationally lensed ultraluminous infrared galaxy SMM J2135−0102 at $z = 2.3$. This is the first detection of ^{13}CO and C^{18}O in a high-redshift star-forming galaxy. These data comprise observations of six transitions taken with Plateau de Bure Interferometer and we combine these with ∼33 GHz Jansky Very Large Array data and our previous spatially resolved ^{12}CO and continuum emission information to better constrain the properties of the interstellar medium (ISM) within this system. We study both the velocity-integrated and kinematically decomposed properties of the galaxy and coupled with a large velocity gradient (LVG) model we find that the star-forming regions in the system vary in their cold gas properties, in particular in their chemical abundance ratios. We find strong C^{18}O emission both in the velocity-integrated emission and in the two kinematic components at the periphery of the system, where the C^{18}O line flux is equivalent to or higher than the ^{13}CO. We derive an average velocity-integrated flux ratio of ^{13}CO/C^{18}O ∼ 1 which suggests an abundance ratio of [^{13}CO]/[C^{18}O] which is at least seven times lower than that in the Milky Way. This is suggestive of enhanced C^{18}O abundance, perhaps indicating star formation preferentially biased to high-mass stars. We estimate the relative contribution to the ISM heating from cosmic rays and UV of (30–3300) × 10^{-25} erg s^{-1} and 45 × 10^{-25} erg s^{-1} per H_2 molecule respectively and find them to be comparable to the total cooling rate of (0.8–20) × 10^{-25} erg s^{-1} from the CO. However, our LVG models indicate high (>100 K) temperatures and densities (>10^3) cm^{-3} in the ISM which may suggest that cosmic rays play a more important role than UV heating in this system. If cosmic rays dominate the heating of the ISM, the increased temperature in the star-forming regions may favour the formation of massive stars and so explain the enhanced C^{18}O abundance. This is a potentially important result for a system which may evolve into a local elliptical galaxy.

Key words: ISM: abundances – ISM: molecules – galaxies: high-redshift – galaxies: starburst – submillimetre: ISM.

1 INTRODUCTION

Cold molecular gas in the interstellar medium (ISM) in galaxies provides the raw materials from which stars can form. The physical properties of the gas determine the range of initial conditions for star formation. In local galaxies the ISM typically exhibits a considerable range of properties, with densities ranging between 10^{0-7} cm^{-3} and temperatures of ∼10–10 000 K. This material is heated by a variety of sources, e.g. the stellar radiation field, turbulence and cosmic rays, and subsequently cools through atomic and molecular line emission. Star formation itself takes place in

⋆ E-mail: a.l.r.danielson@durham.ac.uk

giant molecular clouds (GMCs) where the gas is at its densest ($n(H_2) > 10^4$ cm^{-3}; Gao & Solomon 2004; Bergin & Tafalla 2007) and the temperatures are typically low (10–20 K), making the denser ISM phases the more important to study when it comes to defining the star formation process.

The most abundant molecule in GMCs is hydrogen (H_2); however, since it lacks a permanent dipole and has very low mass, it is very challenging to directly observe, as very high temperatures are required to excite the quadrupolar rotational transitions. This means that cold, star-forming H_2 gas is almost impossible to directly observe in emission. The next most abundant molecule is carbon monoxide ($^{12}C^{16}O$, hereafter ^{12}CO), which has very strong emission lines from pure rotational transitions at millimetre wavelengths. Since the formation of molecular species such as ^{12}CO occurs under similar conditions to H_2 formation, ^{12}CO emission is commonly used as an H_2 tracer species and, with some assumptions, can be used to derive the mass of H_2 likely to be present in the ISM. The lowest ^{12}CO rotational transitions ($J = 1\rightarrow0$ and $2\rightarrow1$, hereafter $J_{up} = 1$ and $J_{up} = 2$) are those typically used for tracing the bulk of the cold gas in galaxies (e.g. Young & Scoville 1991). However, the high optical depth of lines of the main isotopologue, ^{12}CO ($\tau \sim 5$–10 for $J_{up} = 1$), at relatively low column densities, means that in externally heated clouds, ^{12}CO emission is dominated by the warm cloud surfaces, thus limiting the information that can be deduced about the physical properties of the high-density molecular gas. This high optical depth forces the use of an empirical conversion factor (calibrated from local late-type galaxies) in order to deduce cold gas mass from ^{12}CO $J_{up} = 1$ line emission (so-called X_{CO} or α_{CO} factor; see e.g. Dickman, Snell & Schloerb 1986). This factor can vary significantly depending on the average physical and kinematical state of the cold molecular gas (i.e. UV photodissociation rate, gas density, column density, kinetic temperature, metallicity; see Bryant & Scoville 1996). The conversion factor α_{CO} (between gas mass and ^{12}CO line luminosity, $\alpha_{CO} = M_{H_2}/L'_{^{12}CO(1-0)}$) has a value of $\sim$4.6 in the disc of the Milky Way, whereas in local Ultra Luminous Infrared Galaxies (ULIRGs) a significantly lower average value of $\sim$0.8 is generally preferred, though with considerable uncertainty (e.g. Downes & Solomon 1998; Stark et al. 2008; Papadopoulos et al. 2012b).

A more reliable probe of the physical conditions of the cold gas requires measurements of optically thin tracers, capable of probing all of the column. ^{13}CO and $C^{18}O$ (rare isotopologues of CO) can provide this due to their significantly lower abundances (and hence lower optical depths; $\tau < 1$) than ^{12}CO. ^{13}C is a 'secondary' species produced in longer lived, low-to-intermediate mass stars, compared to the 'primary' nature of ^{12}C which is formed in and ejected from high-mass stars (Wilson & Rood 1994). Thus, ^{13}CO is generally associated with the later stages of star formation. Less is known about the origin of the optically thin molecule $C^{18}O$, however, it is generally associated with high-mass star formation and ^{18}O is potentially a major constituent of the winds of massive stars (i.e. Henkel & Mauersberger 1993; Prantzos, Aubert & Audouze 1996). Given the lower abundance of these isotopes (i.e. $[^{12}C]/[^{13}C] \sim 20$–$140$ Martín et al. 2010; $[^{16}O]/[^{18}O] \sim 150$–$200$ Henkel & Mauersberger 1993), ^{13}CO is expected to be optically thin in all but the highest density, highest extinction, star-forming cores. In the densest cores, $C^{18}O$ may provide a better tracer of H_2 due to its lower abundance and optical depth than ^{13}CO. In the Milky Way, the abundance ratio of $[^{13}CO]/[C^{18}O] \sim 7$–$8$ (i.e. Henkel & Mauersberger 1993).

Whilst these isotopologues may provide more robust measurements of the star-forming gas, their low abundances mean that they are very difficult to detect at high redshift. Indeed, the only high-redshift detection of ^{13}CO and $C^{18}O$ is from the Cloverleaf quasar (Henkel et al. 2010). However, if detections can be made in star-forming galaxies, then their strengths and line ratios with respect to other isotopologues will provide a diagnostic of the physical conditions of the ISM. For example, GMCs experiencing strong recent star formation may display elevated $C^{18}O$ and ^{12}CO abundances relative to ^{13}CO, in particular in systems preferentially forming massive stars (i.e. Henkel & Mauersberger 1993; Meier & Turner 2004).

Recently, we discovered a bright, lensed sub-mm galaxy at $z \sim 2.3$, SMM J2135−0102 (hereafter SMM J2135, Ivison et al. 2010; Swinbank et al. 2010; Danielson et al. 2011). This galaxy is amplified by a foreground cluster producing three images of the background galaxy, of which the two brightest are seen adjacent to each other reflected across the critical curve. These two images have a combined amplification of 37.5 times, resulting in an apparent 870 μm flux of 106 ± 3 mJy. Hence, intrinsically the galaxy has an unlensed 870 μm flux of $\sim$3 mJy and a far-infrared luminosity of $\sim 2.3 \times 10^{12}$ $L_\odot$ equivalent to a star formation rate (SFR) of ~ 400 $M_\odot$ yr^{-1} (comparable to the local ULIRG Arp 220).

Danielson et al. (2011) obtain very high signal-to-noise (S/N) detections of 11 transitions from three molecular and atomic species (^{12}CO, [C I] and HCN) and limits on a further 20 transitions from nine species in SMM J2135. The ^{12}CO line profiles show multiple kinematic components with different excitation temperatures. Swinbank et al. (2011) probe the high-resolution kinematics of the system, identifying four dense star-forming clumps (with physical scales of $\sim$100–200 pc) which closely correspond to the kinematic components. These clumps are embedded within a rotationally supported disc, $\sim$5 kpc in diameter. Moreover, Danielson et al. (2011) show that the cold molecular gas associated with the star formation appears to be exposed to UV radiation fields 10^4 times more intense than in the Milky Way and suggest that photon heating should dominate in the source. However, there have been various studies which have suggested that in galaxies with high SFR densities (and hence high supernova rates), heating due to cosmic rays may play a very significant role in the heating of the H_2 gas (e.g. Goldsmith & Langer 1978; Bradford et al. 2003; Hailey-Dunsheath et al. 2008; Bayet et al. 2011a,b). In particular, Papadopoulos (2010) demonstrates the importance of cosmic ray heating over photon heating in ULIRGs with high densities and high SFRs. In these systems, cosmic rays are capable of penetrating the dense star-forming gas clumps and volumetrically heating the gas, resulting in kinetic temperatures 8–16 times higher than in UV-shielded star-forming cores in the ISM of ULIRGs, which in turn can alter the conditions for star formation and thus the characteristic mass of stars.

In this paper, we extend our previous study of SMM J2135 from the ^{12}CO spectral line energy distribution (SLED) analysis to include key $J_{up} = 1$–7, ^{13}CO and $C^{18}O$ line emission, using the Plateau de Bure Interferometer (PdBI) and the Karl. G Jansky Very Large Array[1] (JVLA). We use these data to improve the large velocity gradient (LVG) modelling of this system, and hence to determine the likely physical conditions of the cold molecular gas in the ISM. We compare the ^{13}CO and $C^{18}O$ line profiles with the optically thick ^{12}CO to build a better understanding of the distribution, properties and kinematics of the cold molecular gas in this system. We

[1] The National Radio Astronomy Observatory is a facility of the National Science Foundation operated under cooperative agreement by Associated Universities, Inc.

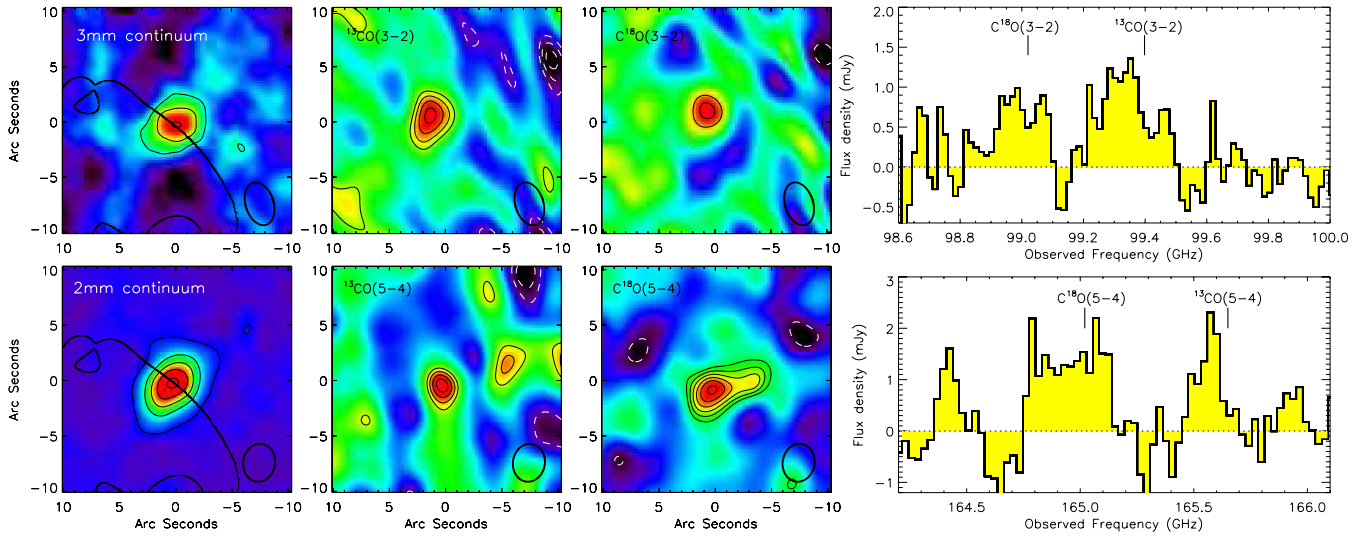

Figure 1. Left and centre: signal-to-noise maps of the continuum and the transitions of $J_{up} = 3$ and $J_{up} = 5$ ^{13}CO and C^{18}O line emission, where the latter two are extracted over the frequency extent of the emission lines. The contours on the continuum maps represent 5, 10, 15σ for the 100 GHz (3 mm) data and 5, 25, 45σ for the 165 GHz (2 mm) data. The black curve through the continuum maps represents the critical curve from the gravitational lensing model (Swinbank et al. 2011). The contours on the line maps represent 3, 4, 5, 6σ etc. The line maps have been continuum subtracted and then slightly smoothed for display purposes. These maps demonstrate that we have significant detections of the continuum and the $J_{up} = 3$ and $J_{up} = 5$ transitions in SMM J2135 and furthermore that the structure and extent of the emission varies between the different transitions. Right: the continuum-subtracted spectra (output from GILDAS) for the $J_{up} = 3$ and $J_{up} = 5$ transitions. The expected central frequencies of the transitions for the heliocentric redshift of $z = 2.325\,91$ are labelled with solid lines. The fluxes given in Table 1 have been determined by integrating the spectra in the velocity range of -350 to $+550\,\mathrm{km\,s^{-1}}$ (the FWZI of the ^{12}CO lines in Danielson et al. 2011). The channel widths are $50\,\mathrm{km\,s^{-1}}$ for both spectra shown.

also estimate the likely heating contributions from cosmic rays and photons in order to determine the dominant heating process.

In Section 2, we describe our observations of the molecular emission from SMM J2135. Our observational analysis and results are described in Section 3 where we first consider the velocity-integrated (hereafter 'integrated') properties of the system, followed by decomposing the source into previously identified kinematic components and deriving their individual cold molecular gas properties. In Section 4, we then use LVG models to further probe the properties of the cold molecular gas. We combine the observational and theoretical findings in Section 5 and discuss the possible physical structure and properties of SMM J2135, as well as considering the dominant heating mechanisms in the source. We give our conclusions in Section 6. Throughout the paper we use a Λ CDM cosmology with $H_0 = 72\,\mathrm{km\,s^{-1}}$ Mpc^{-1}, $\Omega_m = 0.27$ and $\Omega_\Lambda = 1 - \Omega_m$ (Spergel et al. 2003, 2007). We apply a lensing amplification correction of a factor of 37.5 ± 4.5 to any luminosities throughout (see Swinbank et al. 2011 for a summary of the gravitational lensing model).

2 OBSERVATIONS AND REDUCTION

2.1 Plateau de Bure Interferometer Observations

We used the six-element IRAM PdBI[2] with the WIDEX correlator to observe the $J_{up} = 3$, 5 and 7 transitions of ^{13}CO and C^{18}O, and the continuum at ∼100, 165 and 232 GHz, respectively. WIDEX is a dual-polarization correlator with a large bandwidth of 3.6 GHz and a fixed frequency resolution of 2 MHz. Observations were made in the lowest resolution D-configuration between 2011 March 25th and 2011 October 15th. The frequency coverage was tuned to the systemic redshift determined from the ^{12}CO $J = 1\rightarrow0$ (hereafter ^{12}CO(1–0)) discovery spectrum ($z = 2.325\,91$; Swinbank et al. 2010). We integrated until we reached a noise level of ∼0.6 mJy per $40\,\mathrm{km\,s^{-1}}$ channel in the 100 GHz and 165 GHz observations and ∼0.8 mJy per $50\,\mathrm{km\,s^{-1}}$ in the 232 GHz data. The overall flux scale for each observing epoch was set by MWC 349 for a majority of the observations, with additional observations of 2134+004 for phase and amplitude calibrations, due to the presence of a strong radio recombination line in the emission from MWC 349 at 232 GHz. The data were calibrated, mapped and analysed using the GILDAS[3] software package. During the mapping process natural weighting was applied. For natural weighting, beam sizes and position angles were determined to be 4.0 arcsec × 2.5 arcsec and PA = 17°.0, 3.4 arcsec × 2.8 arcsec and PA = 171°.0, and 3.4 arcsec × 2.1 arcsec and PA = 2.3°, for the 100, 165 and 232 GHz data, respectively.

We show in Fig. 1 the S/N maps for the ^{13}CO and C^{18}O observations. The continuum maps are produced by measuring the median over the off-line continuum in every spatial pixel and dividing it by the standard deviation of the continuum in the same frequency range. To create the line maps, we fit the continuum with a low-order polynomial in every spatial pixel and subtract it from the cube, we then produce a collapsed image over the full width at zero intensity (FWZI) frequency range of the line (see below). We then produce S/N maps from this by dividing the signal by the product of the standard deviation of the continuum and the square root of the number of frequency channels in the line. In Fig. 2, we show the spectra of ^{13}CO and C^{18}O. The 1D spectra are produced by integrating within an aperture around the full extent of the emission

[2] Based on observations carried out with the IRAM Plateau de Bure Interferometer under programme u0b6. IRAM is supported by INSU/CNRS (France), MPG (Germany) and IGN (Spain).

[3] http://www.iram.fr/IRAMFR/GILDAS/

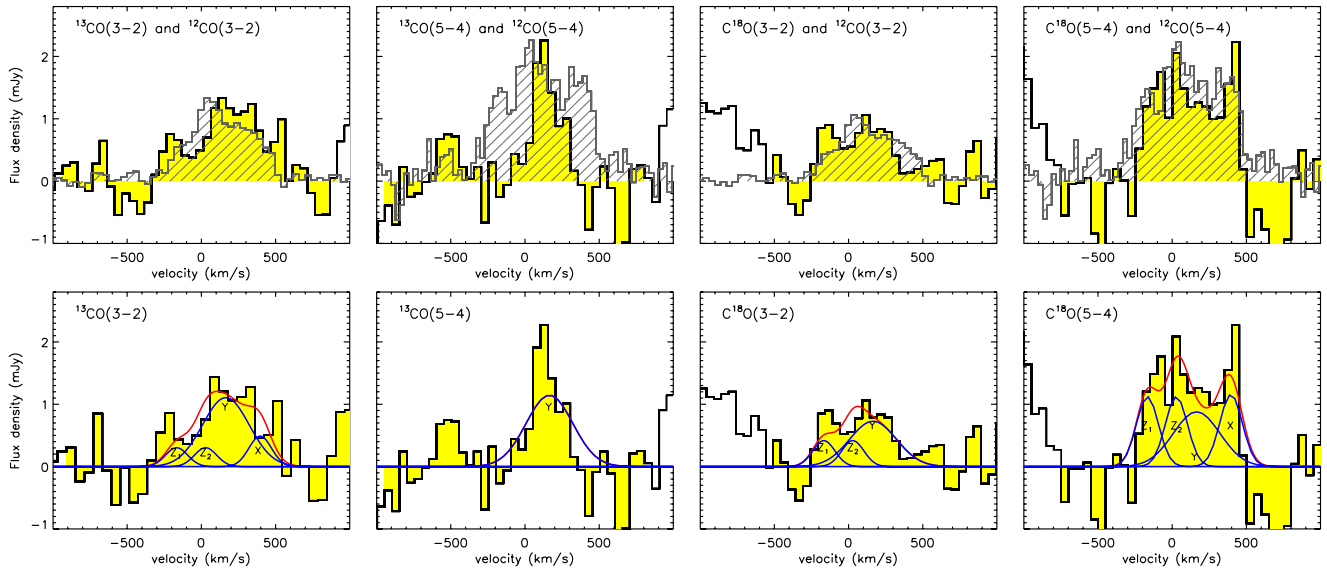

Figure 2. Top row: continuum-subtracted spectra for the individual transitions (filled histograms) plotted to compare the line profiles of the ^{13}CO and C^{18}O. Overlaid on each is the spectrum for the, respective, ^{12}CO transition (normalized by peak flux) to compare the velocity structure (hatched region). Bottom row: the spectra for all lines, with the three-component kinematic model with components *X*, *Y*, *Z*, taken from the Danielson et al. (2011) fit to each line (see Section 3.2 and Fig. 3). The channel widths are 50 km s^{-1} for the ^{13}CO and C^{18}O but 40 km s^{-1} and 30 km s^{-1} for the ^{12}CO(3–2) and (5–4), respectively. In each case, the continuum was fitted with a low-order polynomial and subtracted from the one-dimensional spectrum output by GILDAS. It is clear that the line profiles differ strongly between the different species. This is likely to be due to a combination of factors, potentially including differences in optical depth and abundance. The three-component kinematic fit to the spectra demonstrates that the different transitions are dominated by different kinematic components, i.e. only the *Y*-component is required to fit the ^{13}CO(5–4) line.

region in the cleaned cube. We note that the S/N maps and spectra of ^{13}CO and C^{18}O shown in Figs 1 and 2 are continuum subtracted.

Inspection of the velocity-integrated data cubes (Fig. 1) shows strong detections (S/N∼4–8) for ^{13}CO(3–2), ^{13}CO(5–4), C^{18}O(3–2) and C^{18}O(5–4), although we only detect continuum at 232 GHz (i.e. no ^{13}CO(7–6) or C^{18}O(7–6) detections). Since the spectra are clearly highly structured (see also Danielson et al. 2011), we do not fit a single Gaussian to determine the integrated flux but instead we integrate the spectra in the velocity range of −350 to +550 km s^{-1} (the FWZI of the ^{12}CO composite line in Danielson et al. 2011; see Fig. 3). We note that since some of the line profiles are narrower than others, the S/N of the integrated flux value may appear low due to integrating over the same FWZI for all lines which may not be appropriate for, i.e. the narrow ^{13}CO(5–4) line. For the undetected lines of ^{13}CO(7–6) and C^{18}O(7–6), we determine a 3σ upper limit on the fluxes by assuming a linewidth typical of the average linewidth of the detected lines for the same species (900 km s^{-1}). In Table 1, we provide line fluxes (with associated measurement uncertainties) or limits for the various species and we include the ^{12}CO data from Danielson et al. (2011) for completeness. We estimate additional flux calibration uncertainties of 10 per cent at 100 GHz, 15 per cent at 165 GHz and 20 per cent at 232 GHz, which are taken into account in all analyses on the spectral lines but not included in the tabulated flux and error values.

2.2 JVLA Observations

SMM J2135 was observed with the JVLA in D-configuration between 2011 September and December. The Ka receiver was tuned to 33.13 GHz, covering both the ^{13}CO(1–0) and C^{18}O(1–0) lines. Standard amplitude, phase and bandpass calibration procedures were used. While we wanted to set up our observations with a scan-averaging time of 1 s, National Radio Astronomy Observatory (NRAO) staff instructed us to use a scan-averaging time of 3 s. A

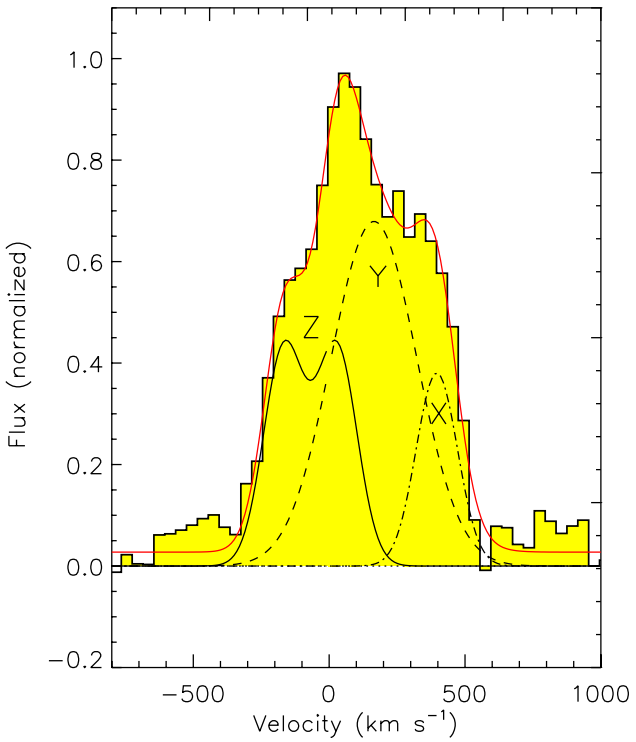

Figure 3. A composite spectrum of the ^{12}CO spectra of SMM J2135 from $J_{up} = 1-8$, normalized by the peak flux, taken from Danielson et al. (2011). This composite is used to define an FWZI range over which to sum the total flux (−350 to 550 km s^{-1}). Furthermore, utilizing the high signal-to-noise of the ^{12}CO emission lines, this composite spectrum is used (in Danielson et al. 2011) to fit and determine the three-component (*X*, *Y* and the double-peaked *Z*) kinematic model plus continuum that we apply to our ^{13}CO and C^{18}O emission lines in this work.

Table 1. Line fluxes and flux ratios for integrated and decomposed spectra.

Species or line ratio	ν_{rest} (GHz)	Integrated flux (Jy km s^{-1})	Kinematically decomposed flux[a, b, c] Z (Jy km s^{-1})	Y (Jy km s^{-1})	X (Jy km s^{-1})
^{13}CO(1–0)	110.2014	<0.07	<0.03	<0.05	<0.03
^{13}CO(3–2)	330.5880	0.66 ± 0.08	0.11 ± 0.06	0.43 ± 0.09	0.09 ± 0.06
^{13}CO(5–4)	550.9263	0.38 ± 0.14[e]	<0.43	0.46 ± 0.07	<0.21
^{13}CO(7–6)	771.1841	<0.41	<0.26	<0.38	<0.26
C^{18}O(1–0)	109.7822	<0.07	<0.03	<0.05	<0.03
C^{18}O(3–2)	329.3305	0.41 ± 0.08	0.16 ± 0.06	0.28 ± 0.09	<0.16
C^{18}O(5–4)	548.8310	0.87 ± 0.16	0.43 ± 0.08	0.34 ± 0.13	0.21 ± 0.09
C^{18}O(7–6)	768.2514	<0.41	<0.26	<0.38	<0.26
^{12}CO(1–0)[d]	115.2712	2.16 ± 0.11	0.56 ± 0.11	1.3 ± 0.2	0.4 ± 0.2
^{12}CO(3–2)[d]	345.7959	13.20 ± 0.10	3.6 ± 0.6	7.6 ± 1.1	2.3 ± 1.1
^{12}CO(4–3)[d]	461.0408	17.3 ± 1.2	3.8 ± 0.8	9.9 ± 1.4	4.0 ± 1.4
^{12}CO(5–4)[d]	576.2679	18.7 ± 0.8	7.2 ± 0.7	7.1 ± 1.3	4.5 ± 1.3
^{12}CO(6–5)[d]	691.4731	21.5 ± 1.1	8.2 ± 0.9	8.7 ± 1.6	5.1 ± 1.6
^{12}CO(7–6)[d]	806.6518	12.6 ± 0.6	4.7 ± 0.5	5.9 ± 0.9	1.1 ± 0.9
^{12}CO(8–7)[d]	921.7997	8.8 ± 0.5	3.2 ± 0.3	3.1 ± 0.6	2.5 ± 0.6
^{12}CO(1–0)/C^{18}O(1–0)	–	>31	>19	>26	>13
^{12}CO(3–2)/C^{18}O(3–2)	–	32 ± 6	23 ± 9	27 ± 10	>15
^{12}CO(5–4)/C^{18}O(5–4)	–	21 ± 4	16 ± 4	21 ± 15	21 ± 17
^{12}CO(7–6)/C^{18}O(7–6)	–	>31	>18	>16	>4
^{12}CO(1–0)/^{13}CO(1–0)	–	>31	>19	>26	>13
^{12}CO(3–2)/^{13}CO(3–2)	–	20 ± 2	32 ± 17	18 ± 5	25 ± 21
^{12}CO(5–4)/^{13}CO(5–4)	–	49 ± 18	>17	15 ± 10	>21
^{12}CO(7–6)/^{13}CO(7–6)	–	>31	>18	>16	>4
^{13}CO(3–2)/C^{18}O(3–2)	–	1.6 ± 0.4	0.69 ± 0.46	1.5 ± 0.6	>0.56
^{13}CO(5–4)/C^{18}O(5–4)	–	0.44 ± 0.18	<1.0	1.3 ± 0.5	<1.0

[a]We quote 3σ limits for all lines which are not formally detected.
[b]Uncertainties on fluxes include measurement errors but do not include the flux calibration uncertainties, which we estimate as ∼10 per cent at 100 GHz, ∼15 per cent at 165 GHz and ∼20 per cent at 232 GHz.
[c]The fluxes in Jy km s^{-1} are observed values.
[d]Fluxes are taken from Danielson et al. (2011), shown here for comparison. Flux calibration uncertainties are estimated to contribute an additional ∼5 per cent for 30–200 GHz and ∼10 per cent for 200–300 GHz.
[e]The S/N of this line appears to be lower than in the line maps in Fig. 1 since the flux is determined by integrating over an FWZI of 900 km s^{-1} for all lines and the ^{13}CO(5–4) line is significantly narrower than the other lines.

bug in the observing software resulted in all the integration time after the first second of every scan being discarded. Thus, two thirds of the data were lost. As a result the JVLA spectrum is shallow (containing only 5 h of integration time) and only provides upper limits on the ^{13}CO(1–0) and C^{18}O(1–0) emission. However, we still use these upper limits as constraints for the modelling in Section 4.

3 ANALYSIS AND RESULTS

We have observed four transitions from ^{13}CO and C^{18}O and detect both these species in their $J_{up} = 3$ and $J_{up} = 5$ transition and place sensitive limits on their $J_{up} = 1$ and $J_{up} = 7$ emission. We combine this information with the previous work of Danielson et al. (2011) to give a combined data set with 11 detections and four limits on ^{12}CO, ^{13}CO and C^{18}O. This is a unique and unprecedented data set for a high-redshift galaxy and allows us to probe the densities, temperatures and chemical abundances within the ISM of this starburst galaxy.

To compare the line profiles between the isotopologues of ^{12}CO and ^{13}CO, in Fig. 2 we overlay the corresponding ^{12}CO transition on the ^{13}CO spectra, normalized by their peak fluxes. It is clear that the different species exhibit very different line profiles and that there are multiple velocity components detected through ^{13}CO and C^{18}O. These differences are particularly prominent in $J_{up} = 5$ in both ^{13}CO and C^{18}O where ^{13}CO(5–4) is significantly narrower than both the C^{18}O(5–4) and the ^{12}CO lines. Furthermore, as Fig. 1 shows, C^{18}O(5–4) appears to be spatially extended along the same direction as the high-resolution ^{12}CO maps (Swinbank et al. 2011) unlike the other lines which are more compact in their spatial distribution.

Considering the unusual profiles, large integrated flux and spatial extent of the C^{18}O(5–4), we test the validity of these data by splitting the sample into two independent data sets of half the exposure time and measure the integrated flux in each half of the data. The S/N in each half of the data is obviously lower than that of the total sample but we find the C^{18}O(5–4) fluxes to be 0.82 ± 0.20 and 0.83 ± 0.25 which are consistent with each other and with the total flux of 0.87 ± 0.16. Furthermore, we find that both the spatial extent and the line profile persist in both samples.

Figs 2 and 4 clearly show the presence of multiple kinematic components with different ^{13}CO and C^{18}O line strengths. In Danielson et al. (2011), we kinematically decompose the ^{12}CO emission line spectra in SMM J2135 into multiple velocity components (i.e. Fig. 3). In Section 3.2, we fit this same model to the ^{13}CO and C^{18}O lines and discuss the kinematically decomposed properties of

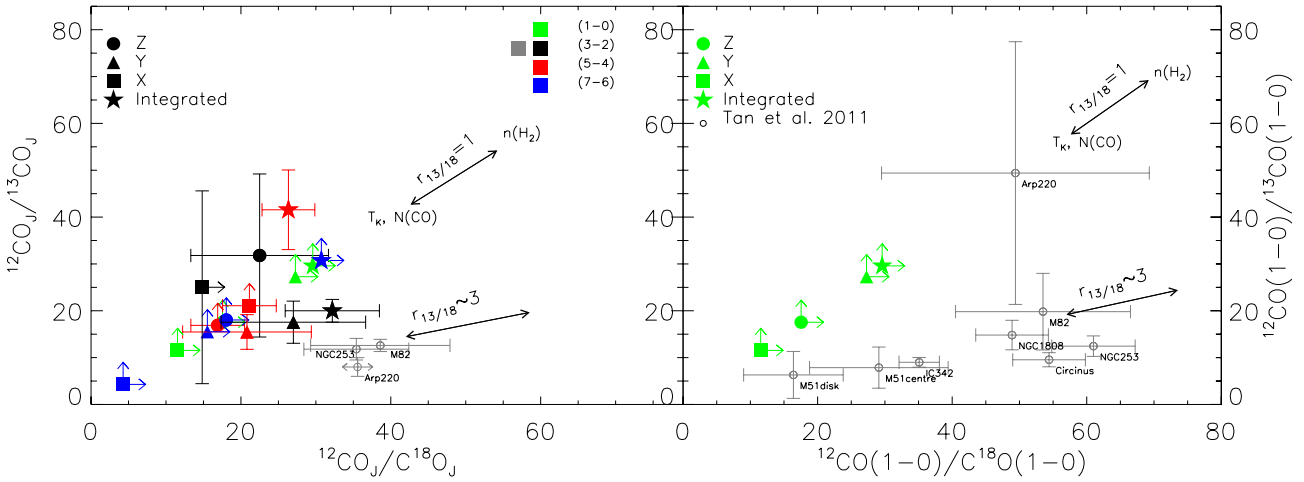

Figure 4. Left: flux ratios of ^{12}CO/^{13}CO versus ^{12}CO/C^{18}O for the integrated emission from SMM J2135 for the different transitions available. We also plot the individual components of the three-component kinematic model. For comparison, we show the flux ratios of the star-forming systems Arp 220 (Greve et al. 2009), M 82 (Petitpas & Wilson 2000) and NGC 253 (Harrison et al. 1999). The literature values are ratios using the $J_{up} = 3$ transition in order to compare directly to our data, however, C^{18}O(3–2) fluxes are only published for M 82 and NGC 253, therefore for Arp 220, ^{12}CO(3–2)/C^{18}O(3–2) is determined by multiplying the known ratio in $J_{up} = 1$ by the ratio of (^{12}CO(3–2)/C^{18}O(3–2))/(^{12}CO(1–0)/C^{18}O(1–0)) ~ 0.72 for M 82. Since the estimate for ^{12}CO(3–2)/C^{18}O(3–2) in Arp 220 is a derived value, we do not give a horizontal error bar but note that there is large uncertainty in this estimate. Our integrated ^{12}CO/C^{18}O flux ratio is consistent with that for M 82, whereas our ^{12}CO/^{13}CO is higher than that for M 82. The vectors demonstrate the effect on the line ratios of varying the temperature (T_K), density (n(H$_2$)) and column density (N(^{12}CO)) in the LVG models described in Section 4 whilst fixing the other parameters in the models at their best-fit values. Increasing the temperature and column density causes a decrease in the line ratios, whereas, increasing the density causes an increase in the line ratios. $r_{13/18}$ is defined as N(^{13}CO)/N(C^{18}O) and we include a vector for a lower column density ratio to demonstrate the effect of decreasing the abundance ratio (see Section 4.4 for details). The different kinematic components appear to fit with different ratios of $r_{13/18} = 1-10$, implying that the ISM conditions may vary between the components. Right: we also show our 3σ lower limits from JVLA for the (1–0) emission in order to compare to a broader range of literature data (Tan et al. 2011). Our data lies at higher ^{12}CO(1–0)/^{13}CO(1–0) than local bright infrared galaxies, with the lower limits on ^{12}CO(1–0)/C^{18}O(1–0) being lower than the lower limits of the local galaxy ratios, implying potentially lower than average ^{13}CO and higher than average C^{18}O (assuming ^{12}CO is optically thick in all cases). This could be a genuine abundance effect.

SMM J2135. However, before attempting to disentangle the internal variations of the ISM conditions within this system, we analyse the integrated properties of the galaxy and attempt to draw some broad conclusions, providing a comparison to our subsequent kinematically resolved analysis.

3.1 Integrated Properties

3.1.1 Integrated line ratios

Fig. 4 shows the integrated flux ratios of ^{12}CO/^{13}CO and ^{12}CO/C^{18}O for SMM J2135. These flux ratios can be used as estimates of the abundance ratios but only if the molecules have the same excitation properties and all lines are optically thin (both of which – as we see later – are unlikely to be true). We compare the integrated flux ratios in SMM J2135 with those of star-forming galaxies and ULIRGs in the nearby Universe. Given that line ratios vary with the transition observed, in order to be consistent, we must compare ratios in $J_{up} = 3$ with literature ratios in $J_{up} = 3$. Published measurements of extragalactic C^{18}O ($J_{up} > 1$) emission are rare and for star-forming galaxies we only have this information for the local starburst galaxy M 82 which Petitpas & Wilson (2000) mapped in $J_{up} = 3$ for ^{12}CO, ^{13}CO and C^{18}O, from which we quote the line ratios from the central position in the galaxy, and for the central 23 arcsec of the starburst NGC 253 from Harrison, Henkel & Russell (1999). In Fig. 4, we also include the measured line ratios in $J_{up} = 5$ and $J_{up} = 7$ in SMM J2135, for completeness. There is a much more extensive galaxy sample available for ^{13}CO and C^{18}O in the $J_{up} = 1$ transition, therefore we also use our limits on $J_{up} = 1$ in order to compare our data more directly to other galaxies. For the literature line ratios of ^{12}CO(1–0)/^{13}CO(1–0) and ^{12}CO(1–0)/C^{18}O(1–0) we use Tan et al. (2011).

Our ^{12}CO/^{13}CO integrated flux ratios for SMM J2135 are $\sim 20 \pm 2$ and >31 in $J_{up} = 3$ and $J_{up} = 1$, respectively, both of which are higher than local star-forming galaxies and ULIRGs. For example, in M 82 (Fig. 4) lower values of ^{12}CO(3–2)/^{13}CO(3–2) $= 12.6 \pm 1.5$ (Petitpas & Wilson 2000) and ^{12}CO(1–0)/^{13}CO(1–0) $= 19.8 \pm 8.17$ (Tan et al. 2011) are found. Furthermore, our integrated ^{12}CO(1–0)/^{13}CO(1–0) ratio lies above that for local infrared luminous sources from Tan et al. (2011). Only Arp 220 has a comparably large value of ^{12}CO(1–0)/^{13}CO(1–0) $\sim 50 \pm 30$.

There are many potential explanations for the observed elevated ^{12}CO/^{13}CO flux ratios: (i) turbulence due to mergers or winds can cause the ^{12}CO line to broaden, thus decreasing the optical depth (τ) of the line and increasing the ^{12}CO/^{13}CO intensity ratio without the need for a change in the relative abundances of the isotopologues (Aalto et al. 1995); (ii) in UV radiation-dominated photodissociation regions on the surfaces of molecular clouds, ^{12}CO, with its higher optical depth, more effectively self-shields than ^{13}CO (and C^{18}O), thus ^{13}CO is more easily photodissociated than ^{12}CO, resulting in an elevated ^{12}CO/^{13}CO ratio. Similarly, C^{18}O is more easily photodissociated than ^{13}CO resulting in a higher ^{13}CO/C^{18}O ratio (Bally & Langer 1982); (iii) as ^{13}C is a secondary product from a later stage of nuclear processing than ^{12}C, age can play a role in determining the ^{12}CO/^{13}CO ratio, such that in systems with many newly forming stars ^{12}CO/^{13}CO can be much higher than in older systems where there has been enough time to synthesize ^{13}C (Henkel et al. 2010). Thus, there is a trend of increasing ^{12}CO/^{13}CO with decreasing metallicity, i.e. ULIRGs, which are characterized by lower metallicity, typically exhibit higher ^{12}C/^{13}C ratios

(Casoli, Dupraz & Combes 1992a; Henkel et al. 1993, 1998; Meier & Turner 2004; Genzel et al. 2012); (iv) Casoli, Dupraz & Combes (1992b) find that the $^{12}CO/^{13}CO$ can be enhanced in regions of recent bursts of star formation, particularly of massive stars, as ^{12}C is overproduced by nucleosynthesis relative to ^{13}C leading to an overabundance of ^{12}CO; (v) similarly, infall of unprocessed gas from the disc into the nuclear region(s) of starbursts may lead to enhanced $^{12}CO/^{13}CO$ ratios; (vi) Finally, chemical fractionation may also affect the observed $^{12}CO/^{13}CO$ ratio, i.e.

$$^{13}C^{+} + ^{12}CO \rightarrow ^{12}C^{+} + ^{13}CO + \Delta E_{35K}, \quad (1)$$

(Watson, Anicich & Huntress 1976), which enhances ^{13}CO relative to ^{12}CO leading to a lower value for $^{12}CO/^{13}CO$.

In contrast to the elevated $^{12}CO/^{13}CO$ flux ratio, as Fig. 4 shows, SMM J2135 appears to have a lower $^{12}CO/C^{18}O$ flux ratio than local infrared luminous galaxies. This implies either a deficiency in ^{12}CO or, more likely, enhanced $C^{18}O$. However, there are a few local systems which display similar characteristics. For example, Meier & Turner (2001) find very low $^{12}CO/C^{18}O$ integrated intensity ratios in the centre of the star-forming galaxy IC 342 ($^{12}CO(1–0)/C^{18}O(1–0) = 24 \pm 7$ in the central trough compared to >110 in the off-arm regions), suggesting a very high abundance of $C^{18}O$ relative to ^{12}CO in the star-forming regions. The mechanism for ^{18}O synthesis is not well understood, however, a high abundance of $C^{18}O$ is thought to be due to the enrichment of $C^{18}O$ from ^{18}O rich, massive star ejecta and winds (i.e. Henkel & Mauersberger 1993; Meier & Turner 2001). Indeed, since ^{18}O is a secondary product produced in massive stars during He-burning by $^{14}N^{18}O$, an overabundance of $C^{18}O$ in systems which are preferentially producing massive stars may be expected [e.g. due to initial mass function (IMF) variations; Henkel & Mauersberger 1993]. However, it is interesting to note that initial nitrogen abundances and therefore metallicities would have to be almost solar to facilitate the production of such large quantities of ^{18}O, which would be unusual at $z = 2.3$.[4]

It is also interesting to note that Papadopoulos, Seaquist & Scoville (1996) find a relatively low average line ratio of $^{13}CO/C^{18}O = 3.3$ in NGC 1068 for $J_{up} = 1$ and infer that this is either due to an intrinsically low [^{13}CO]/[$C^{18}O$] abundance ratio or optical depth effects (even though both ^{13}CO and $C^{18}O$ are generally considered to be optically thin tracers). Similarly, in Arp 220, the line ratio $^{13}CO(1–0)/C^{18}O(1–0)$ is found to be only 1.0 ± 0.3 (Greve et al. 2009).

Thus, our integrated flux ratios of $^{13}CO(3–2)/C^{18}O(3–2) = 1.6 \pm 0.4$ and $^{13}CO(5–4)/C^{18}O(5–4) = 0.44 \pm 0.18$ in SMM J2135 are unusually low compared to those found in local starbursts and ULIRGs. This is likely to imply an enhanced abundance of $C^{18}O$. Fig. 4 demonstrates the abnormality of SMM J2135, particularly with regard to low $^{12}CO/C^{18}O$ ratios, further emphasizing the possibility of a high abundance of $C^{18}O$ implied by the unusually low $^{13}CO/C^{18}O$ line ratios.

3.2 Kinematically resolved properties

3.2.1 Kinematically resolved model

Using high-resolution mapping, Swinbank et al. (2011) demonstrated that the velocity structure in SMM J2135 coincides with the clumpy structure in the disc. Hence the ∼100–200 pc star-forming clumps observed in the Smithsonian Submillimeter Array (SMA) rest-frame 260 μm map coincide with the clumps observed in the cold molecular gas and these in turn correspond with the kinematic components in the high-resolution ^{12}CO spectra (Swinbank et al. 2011).

Table 2. Kinematically decomposed model fit parameters.

Component	v (km s^{-1})	σ (km s^{-1})
Z_2	-167 ± 9	75 ± 8
Z_1	28 ± 9	75 ± 8
Y	165 ± 13	157 ± 17
X	396 ± 9	76 ± 9

Note. Velocities given with respect to the heliocentric redshift of $z = 2.325\,91$.

To decompose the ^{13}CO and $C^{18}O$ lines into multiple kinematic components, we adopt the kinematic model derived from Danielson et al. (2011). This comprises three Gaussian components: X, Y and Z, where the latter is a coupled double Gaussian. This model provides a reasonable approximation of the observed line profiles (Fig. 3). To be consistent with the ^{12}CO analysis, we fix the central velocities and linewidths of the components X, Y and Z to the values derived using ^{12}CO but allow the intensities to vary when fitting to the new observations (see Table 2). However, as in Danielson et al. (2011) the intensities of the double Gaussian describing component Z are tied to be equal. We show this three-component model in Fig. 3. The central velocities of the components are 396, 165, −70 km s^{-1} for the X, Y and Z components, respectively. The best-fit models for ^{13}CO and $C^{18}O$ are overlaid in Fig. 2 and fluxes (and associated errors) derived from the individual components are listed in Table 1. The ^{13}CO and $C^{18}O$ lines are much fainter (typically ∼20−40 times lower) than the ^{12}CO and hence the detections have lower S/N than the previous ^{12}CO decomposition. As a result, there are degeneracies in fitting the three-component model to some of the lines, however, this approach provides a useful means of consistently comparing the data with our previous ^{12}CO decomposition. Some of the components are undetected in certain transitions and we have strong variations in the line ratios between components (see Table 1 and Fig. 4) and in Section 4 we attempt to model these.

There is a moderate amplification gradient across the source, causing the X-component fluxes to appear fainter than the Z-component. This is demonstrated in Swinbank et al. (2011) where the amplification increases across the source from ∼20 to 50 from the X-component to Z-component. However, our kinematic decomposition is not influenced by the differential magnification as the velocities map uniquely to spatial positions in the lens plane and thus to a single magnification factor.

It is clear from Fig. 2 that the line profiles of ^{12}CO, ^{13}CO and $C^{18}O$ display strong variation in the $^{12}CO/^{13}CO$ and $^{12}CO/C^{18}O$ with velocity, possibly tracing variation in the optical depth of ^{13}CO and $C^{18}O$ or abundance variations. To directly compare the lines, we rebin the ^{12}CO, ^{13}CO and $C^{18}O$ spectra in $J_{up} = 3$ and 5 to 100 km s^{-1} channels and in Fig. 5 we plot the variation of these line ratios with velocity over the ∼900 km s^{-1} FWZI of the ^{12}CO. We calculate the ratio of the flux density in each channel ($S_\nu(12)/S_\nu(i)$), where S_ν is the flux density in mJy and i refers to either ^{13}CO or $C^{18}O$. In Fig. 5, we show horizontal bars indicating the central velocity of the individual kinematic components. We see little measurable difference between the line ratios as a function of velocity; however,

[4] Using the mass–metallicity relation for $z \sim 1.5$ galaxies from Stott et al. (2013) we estimate a metallicity for SMM J2135 of $\sim 0.3\,Z_\odot$.

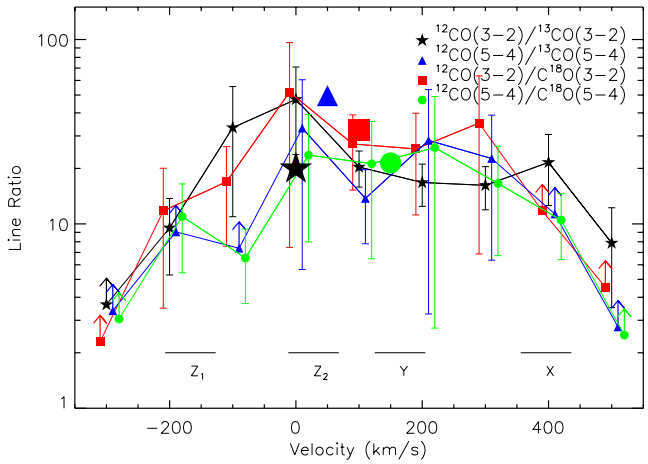

Figure 5. The variation of the estimated line ratios as a function of velocity across the spectral lines of ^{12}CO, ^{13}CO and C^{18}O in the $J_{up} = 3$ and 5 transitions. We have re-binned the spectra into channels of 100 km s^{-1} and offset the data sets by 10 km s^{-1} from each other for clarity. The errors are determined from the standard deviation of the off-line 100 km s^{-1} channels. Lower limits at the edges are due to the ^{13}CO and C^{18}O having a narrower FWZI than the ^{12}CO. These are 3σ lower limits. We indicate the velocity centres of the main kinematic components. Overall there is no strong trend with velocity. The integrated line ratios over the FWZI of 900 km s^{-1} of each line are shown as larger filled symbols placed arbitrarily at 0, 50, 100 and 150 km s^{-1}. They are broadly consistent with each other for all transitions.

there is an overall trend that the line ratios are higher towards the kinematic centre (*Y*) of the source than at the edges.

As shown by Fig. 4 (see also Table 1) the ^{12}CO/^{13}CO, ^{12}CO/C^{18}O and ^{13}CO/C^{18}O line ratios of the individual kinematic components (*X*, *Y*, *Z*) in $J_{up} = 3$ and 5 are all within 1σ of the galaxy-integrated values, aside from the ^{12}CO(5–4)/^{13}CO(5–4) and ^{13}CO(5–4)/C^{18}O(5–4) which are significantly different. This is mainly due to the ^{13}CO(5–4) line being significantly narrower than the other lines and hence in Fig. 2 only the *Y*-component is required to fit the line.

In Fig. 4, we also show vectors which demonstrate the effect of varying the abundance ratio of $N(^{13}\mathrm{CO})/N(\mathrm{C}^{18}\mathrm{O})$ (r_{13}/r_{18}; see Section 4.4 for details). It appears that the integrated source, *X*- and *Z*-components follow the trend of the vector corresponding to $N(^{13}\mathrm{CO})/N(\mathrm{C}^{18}\mathrm{O}) = 1$, whereas the different transitions of the *Y*-component are better fitted with a higher abundance closer to $N(^{13}\mathrm{CO})/N(\mathrm{C}^{18}\mathrm{O}) \sim 3$ which may imply that the ISM conditions vary between the components.

In all components, we find up to $\sim$10$\times$ lower ^{13}CO/C^{18}O flux ratios than the typical value of [^{13}CO]/[C^{18}O] $\sim$ 4 (Wang et al. 2004) found in local star-forming galaxies. This is similar to Arp 220, which exhibits low line ratios of ^{13}CO/C^{18}O $\sim$ 1 at its centre in both $J_{up} = 1$ and 2 (Greve et al. 2009; Matsushita et al. 2009), attributed to a high abundance of C^{18}O arising from a recent starburst. As noted earlier, lower than expected abundance ratios may result from ^{18}O enriched gas being ejected from high-mass stars. Thus, it may imply a bias towards high-mass star formation. The ^{12}C/^{13}C abundance ratio is not affected as much since ^{13}C arises from later stages of lower mass star formation.

4 LVG MODELLING

Whilst the comparison of line ratios of different isotopologues is useful, the degeneracies between density, temperature, optical depth and abundance mean that to better constrain the physical properties of the ISM we need to model the SLEDs. In this section, we investigate both the galaxy-integrated properties and the kinematically resolved component properties to better understand the ISM in this system.

4.1 Model description

In Danielson et al. (2011), we analysed the ^{12}CO SLED to attempt to constrain the physical conditions of the molecular gas in SMM J2135, through LVG modelling (Weiß et al. 2005). Here, we can include in our analysis the lower abundance ^{13}CO and C^{18}O SLEDs in order to better determine the ISM conditions. We therefore use the non-LTE radiative transfer code, RADEX, developed by van der Tak et al. (2007), to model the SLEDs and determine the likely physical conditions within SMM J2135 using our complete ^{12}CO, ^{13}CO and C^{18}O SLEDs. We first apply this analysis to the integrated SLEDs, but then motivated by the strong line ratio differences seen within this source (Section 3.2; Figs 2, 4 and 5) we apply the same approach to the kinematically decomposed SLEDs.

Briefly, RADEX solves the radiative transfer equations by assuming an isothermal and homogeneous medium without large-scale velocity fields and assuming a certain geometry to describe the photon escape probabilities. Three different geometries are available but we choose the model mimicking a uniform expanding sphere (LVG approximation), giving a corresponding escape probability formalism of $\beta_{\mathrm{LVG}} = (1 - \mathrm{e}^{-\tau})/\tau$ (e.g. Goldreich & Kwan 1974). In the model, the equations of statistical equilibrium are iteratively solved, beginning by assuming low τ (optically thin) for all emission lines. To derive the physical parameters using this model, molecular collisional rates are required. We used collisional rates from the Leiden Atomic and Molecular Database[5] as recommended in van der Tak et al. (2007). We assume H_2–CO collisional excitation rates from Flower (2001) and a cosmic microwave background temperature of $\sim$9 K (2.73 K redshifted to $z = 2.3$).

The main input variables in the LVG model we use are: the column density $N(X)$ of the species (X) considered (^{12}CO, ^{13}CO or C^{18}O) in cm^{-2}, the linewidth (FWHM) ΔV for each transition in km s^{-1}, the molecular hydrogen volume gas density $n(\mathrm{H}_2)$ in cm^{-3}, the kinetic temperature T_{K} in K and the abundance ratios (i.e. ^{12}C/^{13}C). These variables must either be fixed or fitted for and are described below. In the following, we describe our method for deriving the best model parameters from our LVG model.

4.2 Input parameter selection

In order to select a suitable velocity gradient (ΔV) we require constraints on the size and structure of the source. From previous work (Swinbank et al. 2010, 2011; Danielson et al. 2011), SMM J2135 appears to comprise at least four 100–200 pc star-forming clumps embedded in a rotating gas disc with a diameter of $\sim$5 kpc. We initially take the average full width at half-maximum (FWHM) of the disc emission ($\sim$500 km s^{-1}) as an estimate of the average velocity field that the gas in the system is experiencing (ΔV). The model outputs velocity-integrated line intensities by multiplying the model-estimated radiation temperature by $1.06 \times \Delta V$ (assuming a Gaussian profile). This initial method is crude given that it assumes uniform excitation conditions throughout the entire source, which given the clear structure in the line profiles is unphysical, however, it

[5] http://www.strw.leidenuniv.nl/~moldata/

is useful to first determine the average molecular gas properties. For each of the species ^{12}CO, ^{13}CO and C^{18}O, we carry out simulations and produce model grids with RADEX for the following parameter ranges: kinetic temperature ranging between T_K = 10–200 K in 10 K steps; gas density ranging between $n(H_2) = 10^3$–10^7 cm^{-3} in 0.5 dex steps and molecular line column densities $N(^{12}CO, ^{13}CO, C^{18}O) = 10^{10}$–$10^{20}$ cm^{-2} in intervals of 0.5 dex. See Bayet et al. (2013) for the choice of input parameters and ranges and for a more complete description of the RADEX model we implement.

4.3 Model outputs

In an ideal situation, where all lines are optically thin, we could make the assumption that the integrated line intensity ratio of ^{12}CO/^{13}CO is equivalent to the ratio of the column densities, $N(^{12}CO)/N(^{13}CO)$, which is equivalent to the atomic abundance ratio [^{12}C]/[^{13}C]. We make this assumption in our analysis but we note that since ^{12}CO has a higher optical depth than ^{13}CO, the measured ^{12}CO/^{13}CO line intensity ratio provides only a lower limit on the actual [^{12}CO]/[^{13}CO] abundance ratio. We do not fix $N(^{12}CO)/N(^{13}CO)$ when searching for the best-fit model but instead we allow it to vary, making it an output of the models in order to determine the best-fit abundance ratio. For each unique set of parameters T_K, $n(H_2)$ and $N(^{12}CO, ^{13}CO, C^{18}O)$, the model outputs are fluxes in cgs units (which we convert to Jy km s^{-1} in order to compare directly to our measured fluxes), excitation temperature T_{ex}, brightness temperature T_b and optical depths for ^{12}CO, ^{13}CO and C^{18}O from J_{up} = 1–18. In order to also search for the optimal abundance ratios we construct a grid of models for all combinations of T, $n(H_2)$, $N(^{12}CO)$, $N(^{12}CO)/N(^{13}CO)$ and $N(^{13}CO/N(C^{18}O)$. We use $N(^{13}CO)/N(C^{18}O)$ as a proxy for the [^{13}CO]/[C^{18}O] abundance ratio. To reduce the number of possible models when searching for the best-fit model we allow only five different discrete values of $N(^{13}CO)/N(C^{18}O)$, ranging between 0.1 and 10 (e.g. Penzias 1983; Zhu, Yang & Wang 2007) and similarly only six discrete values of $N(^{12}CO)/N(^{13}CO)$, ranging between ∼1 and 300 in steps of 0.5 dex. Furthermore, we restrict the allowed parameter space such that the implied source size (Ω_S) of the emitting region has a radius of <5 kpc (the diameter of the galaxy is ∼5 kpc as derived from high-resolution ^{12}CO observations from PdBI and JVLA; Swinbank et al. 2011). We therefore set an upper limit of 5 kpc for the radius of SMM J2135:

$$\Omega_S = L'_{CO} / \left(T_b \Delta V D_A^2\right). \quad (2)$$

This most noticeably restricts the minimum allowed column density of the models to $N(^{13}CO) > 10^{15}$ cm^{-2}.

4.4 Integrated spectral line energy distribution

The LVG analysis from Danielson et al. (2011) showed that the ^{12}CO galaxy-integrated SLED is best-fit by a two-phase model: a 'hot', dense phase ($T_k \sim 60$ K, $n(H_2) \sim 10^{3.6}$ cm^{-3}) likely associated with the four dense star-forming clumps and contributing 60 per cent of the total luminosity over all the ^{12}CO lines, and a 'cold', diffuse ($T_k \sim 25$ K, $n(H_2) \sim 10^{2.7}$ cm^{-3}) phase probably corresponding to an extended gas phase in which the clumps are embedded. We therefore begin by attempting a two-phase fit to the new data to test the effect of the additional constraints of ^{13}CO and C^{18}O SLEDs on the results of the LVG modelling.

For this two-phase fit, we first split the large model grid into 'cold' and 'hot' models with a divide at 50 K and search the grid for the optimum combination of 'cold' models and 'hot' models using a χ^2 calculation. We identify the best two-phase model with the minimum χ^2 value then find those two-phase models for which the predicted ^{12}CO, ^{13}CO and C^{18}O SLEDs are within $\Delta\chi^2 = 1\sigma$ of the best fit. In fitting the SLEDs with two phases simultaneously, we have a total of six degrees of freedom per ISM phase: $n(H_2)$, T_K, $N(^{12}CO)$, $N(^{12}CO)/N(^{13}CO)$, $N(^{13}CO)/N(C^{18}O)$ and a normalization factor. For 12 degrees of freedom, we therefore have a 1σ confidence limit of $\Delta\chi^2 = 13.7$. Our general formula for calculating χ^2 is

$$\chi^2 = \sum_{n=1-7} (^{i}CO_{J=n} - ^{i}CO_{model,J=n})^2 / (\alpha_{^{i}CO_{J=n}})^2, \quad (3)$$

where ^{i}CO represents either ^{12}CO, ^{13}CO or C^{18}O, J_{up} = 1, 3, 5, 7 for ^{13}CO and C^{18}O and J_{up} = 1, 3, 4, 5, 6, 7, 8 for ^{12}CO. We include our upper limits on J_{up} = 1 and 7 as constraints in the χ^2 fitting, setting the value to $(2 \pm 1)\sigma$ (in Figs 6 and 8 we show these data as 2σ upper limits). In this equation $\alpha_{^{i}CO_{J=n}}$ represents the error on the line flux constraints.

The measured SLEDs for the three species are shown in Fig. 6 and we show the best-fit combination of 'hot' and 'cold' models. Table 3 gives the best-fit parameters and range of allowed parameters for models that lie within $\Delta\chi^2 = 13.7$ of the best fit. The best-fit parameters for the 'cold' and 'hot' phases respectively are: $\chi^2_{reduced} = 4.1$, $N(^{13}CO)/N(C^{18}O) = 10^{0.5}$ and 10^0, $n(H_2) = 10^3$ cm^{-3} and 10^4 cm^{-3}, $N(^{12}CO)/N(^{13}CO) = 10^2$ for both phases, $N(^{12}CO) = 10^{19.5}$ cm^{-2} and 10^{20} cm^{-2} and T_K = 50 K and 90 K. The addition of the constraints of ^{13}CO and C^{18}O seems to require models with higher temperatures than those found in Danielson et al. (2011) (25 K and 60 K) but the densities are similar ($n(H_2) = 10^{2.7-3.6}$ cm^{-3}). It is important to note that there is degeneracy in the temperature and density such that it is possible that an optimal solution in fact lies at higher density and lower temperature or lower density and higher temperature. To demonstrate this effect we fix all the model parameters at their optimized values and determine the effect of varying each parameter in the models in turn. This is shown by the vectors in Fig. 4 (r_{13}/r_{18}) which show that increasing the temperature and column density causes a decrease in the line ratios of ^{12}CO/^{13}CO and ^{12}CO/C^{18}O, whereas, increasing the density causes an increase in the line ratios. The $N(^{13}CO)/N(C^{18}O)$ ratios for both the 'hot' and 'cold' phases imply that throughout the system (and particularly in the 'hot' phase) there may be an enhanced C^{18}O abundance compared to star-forming galaxies locally.

We note that although these are the best-fit values, a large range of parameters is allowed within $\Delta\chi^2 = 13.7$ of the best-fitting model. This large range of parameters is demonstrated by Fig. 7 where we plot likelihood contours representing the models that lie within $\Delta\chi^2 = 1$ and 2σ of the best fit. For the 'cold' phase, $n(H_2)$ is at the lower limit of the allowed parameter space and for the 'hot' phase $N(^{12}CO)$ is at the upper limit of the allowed parameter space, which means that the best-fit model may in fact require even higher $N(^{12}CO)$ and lower $n(H_2)$, making it difficult to make firm conclusions. However, we note that we initially selected an upper limit of $N(^{12}CO) = 10^{20}$ cm^{-2} for our parameter space, as a higher column density than this would imply extreme values of $N(H_2)$. We also caution that since the errors on the ^{12}CO fluxes are smaller and there are more measured fluxes for ^{12}CO than for the less abundant species, we are slightly weighted towards the ^{12}CO data when searching for an optimum model. Since in Danielson et al. (2011) we derived lower temperature and densities for the two phases than we derive here, this may imply that giving the ^{12}CO SLEDs more weighting may bias the temperature and density towards lower values.

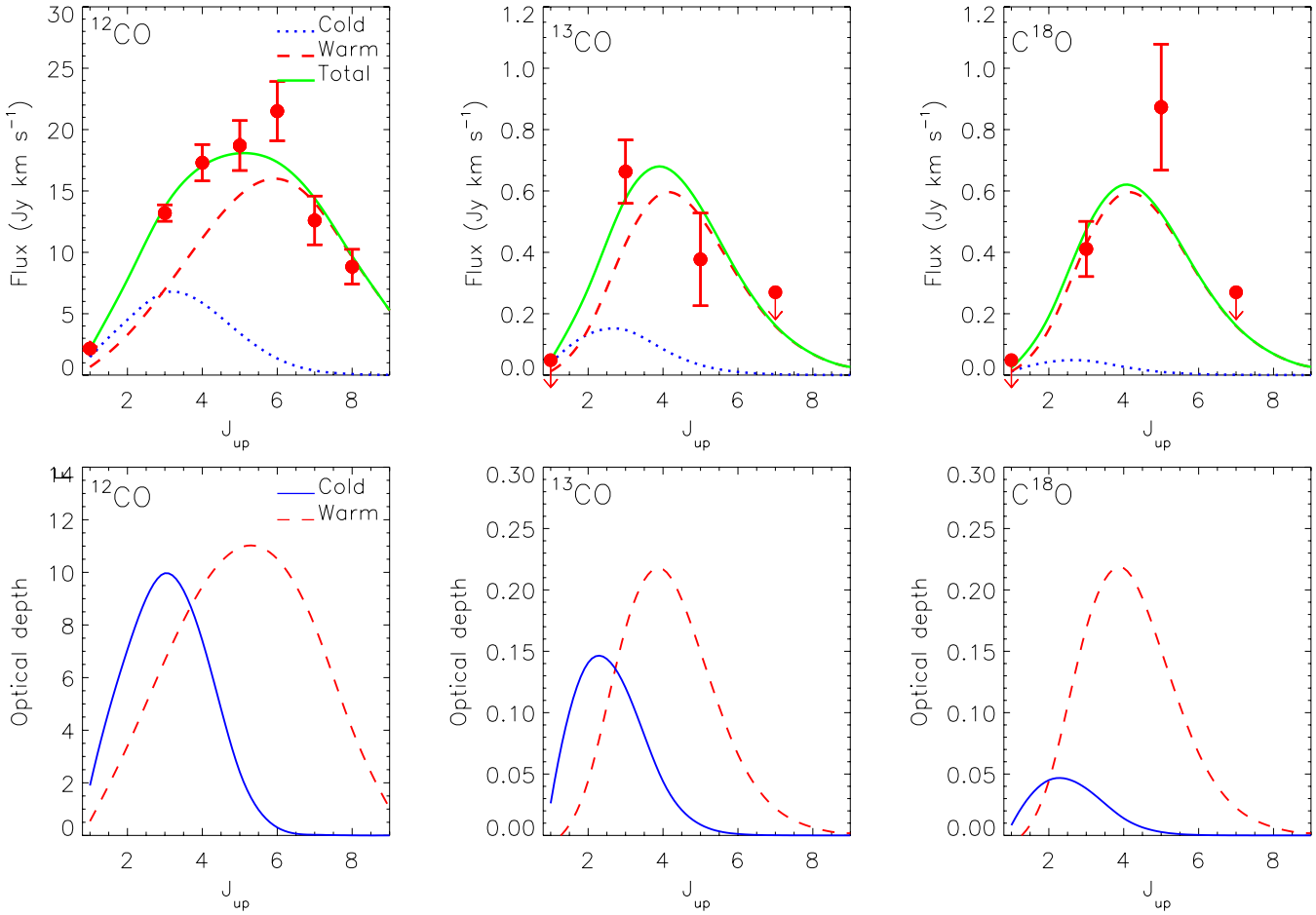

Figure 6. Top: SLEDs for the integrated ^{12}CO, ^{13}CO and C^{18}O emission from SMM J2135. The green solid curve is the best two-phase LVG fit to the SLEDs for all three species at once (described in Section 4). Also shown are the constituent 'hot' and 'cold' phases in red-dashed and blue-solid curves, respectively. Upper limits shown are at a 2σ level for the undetected lines. Bottom: the distribution of the optical depth values for the best-fit 'cold' and 'hot' phases shown as blue-solid and red-dashed curves, respectively.

Table 3. LVG model parameters.

Component	Method	log $\frac{N(^{13}\mathrm{CO})}{N(\mathrm{C}^{18}\mathrm{O})}$	T_K (K)	$n(\mathrm{H_2})$ (cm^{-3})	$N(^{12}\mathrm{CO})$ (cm^{-2})	log $\frac{N(^{12}\mathrm{CO})}{N(^{13}\mathrm{CO})}$	χ^2(reduced)
Search ranges:	–	0.1–1	10–200	10^{3-7}	10^{15-20}	$10^{0-2.5}$	–
Cold	2-phase	0.5 (−1–1)	50 (10–50)	10^3 (10^{3-7})	$10^{19.5}$ (10^{18-20})	2 (0.5–2.5)	4.1
Warm	2-phase	0 (−1–1)	90 (60–160)	10^4 ($10^{3.5-7}$)	10^{20} ($10^{18.5-20}$)	2 (1.5–2.5)	4.1
X	3-component	0 (−0.5–0.5)	200 (30–200)	10^3 (10^{3-7})	10^{19} (10^{15-20})	2 (1.5–2.5)	1.8
Y	3-component	0.5 (0–0.5)	140 (110–200)	$10^{3.5}$ ($10^{3-3.5}$)	$10^{18.5}$ ($10^{18-18.5}$)	1.5 (1.5)	2.5
Z	3 component	0 (−0.5–1)	140 (30–200)	$10^{3.5}$ (10^{3-7})	10^{19} ($10^{18-19.5}$)	2 (1.5–2.5)	3.4

Notes. For kinetic temperature (T_K), H_2 density ($n(\mathrm{H_2})$) and column density ($N(^{12}\mathrm{CO})$), we give the parameter values associated with the minimum χ^2 and the range in these parameters (within $\Delta\chi^2 = 1\sigma$) is given in parentheses. The χ^2 of the two-phase fit is based on 15 data points and 12 free parameters therefore to calculate the reduced χ^2 we divide by 3 degrees of freedom. Similarly for the kinematically decomposed models the reduced χ^2 is calculated by dividing by 9 degrees of freedom (15 data points–6 free parameters).

Since the models we employ also contain optical depth as part of the output, in Fig. 6 we also show the optical depth for each transition of ^{12}CO, ^{13}CO and C^{18}O for the best-fit 'hot' and 'cold' phases. This demonstrates that ^{12}CO is substantially optically thicker (∼50 times) than the ^{13}CO and C^{18}O, as expected. Furthermore, they demonstrate that the 'hot' phases are all optically thicker than the 'cold' phase. This is particularly prominent for the C^{18}O for which the 'hot' phase has a >4 times higher optical depth than the 'cold' phase, however, they would both still be classed as optically thin as $\tau \ll 1$.

With the species abundance ratios and temperatures derived from RADEX we can now estimate the gas mass of SMM J2135 using the

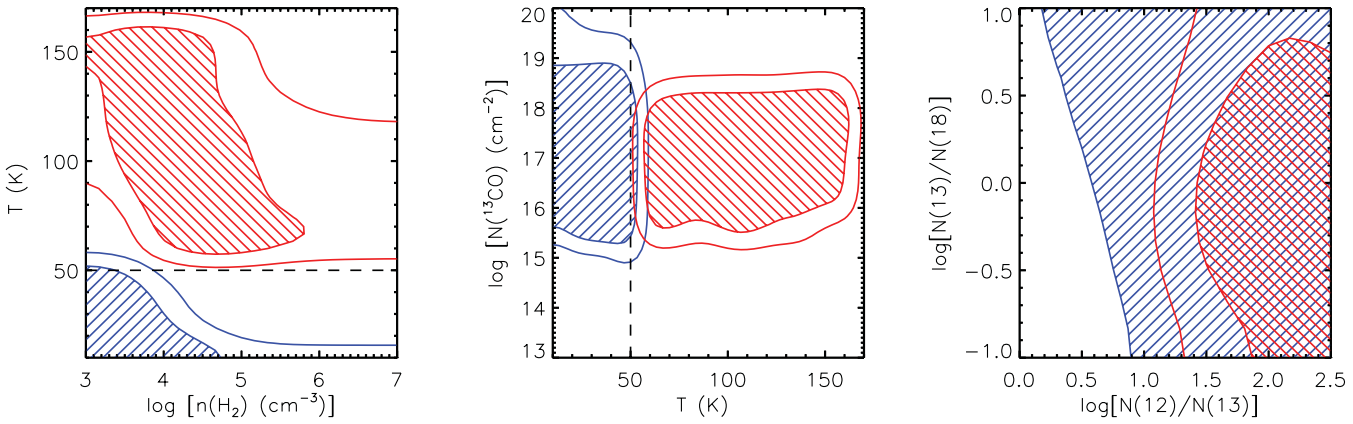

Figure 7. Parameter space distributions of the best-fit 'cold' (blue) and 'hot' (red) phases for different combinations of parameters. The contours represent the models lying within $\Delta\chi^2 = 1$ and 2σ which for 12 degrees of freedom corresponds to models within $\Delta\chi^2$ of 13.7 and 21.3, respectively. The dotted lines on the left and middle plots demonstrate that for the two-phase model fits we restricted the 'cold' phase to have $T \leq 50$ K and for the 'hot' phase we required that it have $T > 50$ K. The hashed regions show the region of parameter space occupied by all the models within $\Delta\chi^2 = 1\sigma$ of the best-fit model. Since there are a large number of degrees of freedom compared to the number of data points we have relatively poor constraints on the allowed parameter space. This provides further motivation to kinematically decompose the emission to test if we can better constrain the parameter space of the individual kinematic components.

optically thin ^{13}CO emission and compare this to previous estimates based on ^{12}CO in Danielson et al. (2011).

4.4.1 Gas mass

In Danielson et al. (2011), we used the ^{12}CO(1–0) line luminosity and the ^{12}CO SLED to constrain an LVG model which predicted a total cold molecular gas mass of $M_{\rm gas} \sim 1.4$–$4.0 \times 10^{10}\,{\rm M}_\odot$ for SMM J2135. This suggested that the empirical conversion factor between CO luminosity and gas mass ($\alpha_{\rm CO} = M_{\rm H_2}/L'_{^{12}{\rm CO}(1-0)}$) is likely to be $\alpha_{\rm CO} \sim 2$ for this system, which is higher than the canonical $\alpha_{\rm CO} \sim 0.8$ normally assumed for high-redshift ULIRGs. Swinbank et al. (2011) use high-resolution mapping of the ^{12}CO(6–5) emission to develop a kinematic model for SMM J2135 and estimate a dynamical mass of $M_{\rm dyn} = (6.0 \pm 0.5) \times 10^{10}\,{\rm M}_\odot$ within ∼5 kpc. Together with an estimated stellar mass of $M_* = (3 \pm 1) \times 10^{10}\,{\rm M}_\odot$ (Swinbank et al. 2010) this suggests a cold molecular gas mass of $M_{\rm gas} \lesssim 4.5 \times 10^{10}\,{\rm M}_\odot$, which is consistent with our predictions from the LVG analysis in Danielson et al. (2011).

However, constraints on the total mass of the H_2 reservoir can be derived using measurements of ^{13}CO and $C^{18}O$, with the advantage that these lower abundance species are expected to be optically thin and so able to trace the bulk of the cold molecular gas including the denser gas typically not probed by ^{12}CO emission. Of course, it is still necessary to assume an abundance ratio between these less abundant isotopologues and H_2 in order to use our measured fluxes to determine the cold gas masses.

To estimate the masses we must first determine the intrinsic source brightness temperature. The integrated line intensity is $I_{\rm CO} = \int T_{\rm mb}\,{\rm d}V$ (K km s^{-1}), and is obtained from the beam-diluted brightness temperature. This must be corrected for the redshift in order to get the velocity-integrated source brightness temperature. Following Solomon et al. (1997), where the line luminosity is $L'_{\rm CO} = T_{\rm b}\Delta V \Omega_{\rm S} D_{\rm A}^2$, we derive a velocity-integrated source brightness temperature of $T_{\rm b}\Delta V = L'_{\rm CO}/\Omega_{\rm S} D_{\rm A}^2$, where $\Omega_{\rm S}$ is the solid angle subtended by the source (in steradians) and $D_{\rm A}$ is the angular size distance (in parsecs). The line luminosity can be calculated from our observed quantities via:

$$L'_{\rm CO} = 3.25 \times 10^7 S_{\rm CO}\Delta V \nu_{\rm obs}^{-2} D_{\rm L}^2 (1+z)^{-3}/\mu ({\rm K\,km\,s^{-1}\,pc^2}), \quad (4)$$

where $S_{\rm CO}\Delta V$ is the velocity-integrated flux density in Jy km s^{-1}, $\nu_{\rm obs}$ is the observed frequency of the transition considered in GHz, $D_{\rm L}$ is the luminosity distance in Mpc and μ is the amplification factor due to gravitational lensing of $\mu = 37.5 \pm 4.5$.

To derive the mass we use

$$M_{\rm H_2} = N_{\rm H_2}\mu_{\rm G} m_{\rm H_2} \Omega_{\rm S} D_{\rm A}^2, \quad (5)$$

where $m_{\rm H_2}$ is the molecular mass of hydrogen (3.346×10^{-27} kg), $\mu_{\rm G}$ is the mean atomic weight of the gas (1.36; including the contribution from helium assuming a 24 per cent helium mass abundance; Scoville et al. 1986) and $N_{\rm H_2}$ is the column density in cm^{-2}. We calculate $N_{\rm H_2}$ following Meier & Turner (2004):

$$N({\rm H_2})_{^i{\rm CO}} = {\rm A} \times \frac{[{\rm H_2}]}{[^{12}{\rm CO}]} \frac{[^{12}{\rm CO}]}{[^i{\rm CO}]} \frac{{\rm e}^{^iE_{\rm u}/T_{\rm ex}}}{{\rm e}^{^iE_{\rm u}/T_{\rm ex}} - 1} {\rm I}_{^i{\rm CO}}, \quad (6)$$

assuming these species to be optically thin and assuming local thermal equilibrium (LTE) for all levels. Here $I_{^i{\rm CO}}$ is the velocity-integrated source brightness temperature of the chosen transition in the chosen species i (in K km s^{-1}); $^iE_{\rm u}$ is the rotational energy ($h\nu/k = 5.5$ K for $J_{\rm up} = 1$); we adopt an average abundance ratio of $[^{12}{\rm CO}]/[{\rm H_2}] = 8.5 \times 10^{-5}$ (Galactic value; Frerking, Langer & Wilson 1982) and A is a constant determined following Scoville et al. (1986):

$$A = \frac{3k}{8\pi^3 B \mu^2} \frac{{\rm e}^{hBJ_1(J_1+1)/kT_{\rm ex}}}{(J_1+1)}, \quad (7)$$

where B is the rotational constant (5.5101×10^{10} s^{-1}) and μ is the permanent dipole moment ($\mu = 0.1098$ Debyes for ^{13}CO where 1 Debye $= 10^{-18}$ g$^{1/2}$ cm$^{5/2}$ s^{-1}). Since $I_{^i{\rm CO}} = T_{\rm b}\Delta V = L'_{\rm CO}/\Omega_{\rm S} D_{\rm A}^2$ the mass equation therefore simplifies to

$$M_{\rm H_2} = A \times \mu_{\rm G} m_{\rm H_2} \frac{[{\rm H_2}]}{[^{12}{\rm CO}]} \frac{[^{12}{\rm CO}]}{[^i{\rm CO}]} \frac{e^{^iE_{\rm u}/T_{\rm ex}}}{e^{^iE_{\rm u}/T_{\rm ex}} - 1} L'_{\rm CO}, \quad (8)$$

where $L'_{\rm CO}$ must be converted into K km s^{-1} cm^2.

From the LVG modelling we predict best-fit values of the excitation temperature of ^{13}CO(3–2) of $T_{\rm ex} = 11.3$ K (with a 1σ range of 9.1–16.8 K) for the cold component and $T_{\rm ex} = 35.4$ K (with a 1σ range of 18.9–155.3 K) for the warm component. Our best-fit value of the abundance ratio of $[^{12}{\rm CO}/^{13}{\rm CO}]$ is ∼100 for both the cold

and warm components. This is significantly higher than the values typically assumed for starburst galaxies of $[^{12}CO]/[^{13}CO] = 40$ (Henkel & Mauersberger 1993; Wilson & Rood 1994). However, we note that there is considerable uncertainty in the abundance ratio within the models on which the derived mass depends strongly. Furthermore, there are strong variations even within galaxies. For example, within the Milky Way the $^{12}C/^{13}C$ atomic abundance ratio varies from ∼20 in the Galactic Centre to >100 in the outer parts of the Galaxy (Wilson & Rood 1994; Wouterloot & Brand 1996). Generally, starburst galaxies and ULIRGs exhibit a $^{12}C/^{13}C > 30$ (e.g. Henkel & Mauersberger 1993; Henkel et al. 2010). However, in the starburst galaxy, M 82, $^{12}C/^{13}C \gtrsim 140$ (Martín et al. 2010).

If we calculate a mass for the warm and cold components separately, using our best-fit value for $[^{12}CO]/[^{13}CO]$, we find $M_{H_2}^{warm} = (5.4–7.2) \times 10^9\,M_\odot$ and $M_{H_2}^{cold} = (2.1–7.8) \times 10^9\,M_\odot$ giving a range in total mass of $M_{H_2} = (0.8–1.5) \times 10^{10}\,M_\odot$ with the hot and cold components contributing approximately equally to the total mass. However, clearly there is uncertainty in the abundance ratio used. Indeed, if we take the maximum abundance ratio within 1σ of the best fit ($[^{12}CO]/[^{13}CO] \sim 300$) we derive an upper limit on the best-fit total mass of $M_{H_2} \sim 2.5 \times 10^{10}\,M_\odot$. The upper limits of this estimate of H_2 mass (derived from $^{13}CO(3–2)$) are consistent with the dynamical limits on M_{gas} derived by $M_{dyn} = M_* + M_{gas}$, with $M_* = (3 \pm 1) \times 10^{10}\,M_\odot$ and $M_{dyn} = (6.0 \pm 0.5) \times 10^{10}\,M_\odot$ (Swinbank et al. 2011; neglecting the contributions of dark matter which is not expected to be dynamically dominant on these scales in a high-redshift galaxy).

Finally, we caution that the magnification factor that we apply is a luminosity-weighted galaxy-integrated factor, however, due to the critical curve passing through SMM J2135, there is a moderate amplification gradient across the source. This is demonstrated in Swinbank et al. (2011) where the amplification increases across the source from ∼20–50. However, the ^{13}CO line that we are using to estimate the gas mass covers the full velocity range of the source and therefore the integrated magnification we use is probably appropriate.

4.5 Kinematically resolved SLEDs

It can be seen from Fig. 6 that in both the ^{12}CO and $C^{18}O$ SLEDs the best-fit model does not peak as high in J_{up} as the data. In Danielson et al. (2011), the model fit peaked at $J_{up} = 6$ whereas adding in the constraints of ^{13}CO and $C^{18}O$ results in a poorer fit to the high-excitation end of the ^{12}CO SLED. Fundamentally, the problem is that if the ^{13}CO and $C^{18}O$ emission are both optically thin, then the difference in their SLED profiles implies that they are not tracing the same gas and therefore, even two-phase LVG models will struggle to fit both species simultaneously. Furthermore, while it is possible to find suitable fits to the data using a two-phase fit, it is difficult to constrain the allowed parameter space due to the large number of degrees of freedom. The velocity structure in the lines suggests multiple components (Figs 2 and 4) and high-resolution mapping of SMM J2135 demonstrates that the velocity structure in SMM J2135 coincides with the clumpy structure observed in the disc (Swinbank et al. 2011). This therefore motivates us to carry out LVG modelling using the SLEDs derived from our kinematic decomposition. However, since we are now considering subcomponents within our system, we must employ a ΔV according to the physical scale of the clumps. The gas clumps identified by Swinbank et al. (2011) are ∼100–200 pc across and have an average FWHM of $\sim 200\,km\,s^{-1}$. However, given that these clumps are likely to be comprised of much smaller structures, the average velocity that the gas in the clumps is experiencing is likely to be much lower than their overall FWHM. We therefore search for models with a $\Delta V = 50\,km\,s^{-1}$. We include the same constraints as before in the χ^2 fitting but since we do not have the S/N or enough data points to do a two-phase fit to each kinematic component we use a single-phase fit to each velocity component with a total of six degrees of freedom: $n(H_2)$, T_K, $N(^{12}CO)$, $N(^{12}CO)/N(^{13}CO)$, $N(^{13}CO)/N(C^{18}O)$ and normalization factor. The six degrees of freedom give a 1σ confidence limit of $\Delta\chi^2 = 7.0$. Again, if we do not detect a component in a particular transition, we include upper limits as constraints, setting the value to $(2 \pm 1)\sigma$.

In Fig. 8, we show the best LVG model fits to the individual kinematic components in SMM J2135. The corresponding best-fit parameters and possible ranges of values within $\Delta\chi^2 = 1\sigma$ of the best fit are listed in Table 3. In Fig. 9, we show the parameter space of our five model parameters with likelihood contours that represent the models that lie within $\Delta\chi^2 = 1$, 2 and 3σ of the best fit. We can better constrain the physical parameters when we fit to each kinematic component individually. The different components occupy different regions of parameter space in temperature, density and column densities. We now discuss the properties of the individual kinematic components.

X-component – this component has a velocity offset from the dynamical centre of the system by $+400\,km\,s^{-1}$. Unfortunately, as a result of it only being detected in $^{13}CO(3–2)$ and $C^{18}O(5–4)$ the ISM properties we derive for this component are very poorly constrained. Broadly, it has a temperature which is only constrained to lie between 30 and 200 K, a density range of $n(H_2) = 10^{3-7}\,cm^{-3}$ and the same high abundance ratio of $N(^{13}CO)/N(C^{18}O) = 1$ as for the *Z*-component.

Y-component – this component is the centre of mass of the system, lying at $+165\,km\,s^{-1}$. It is present in all the observed emission lines in our data set but it is marginally stronger in the ^{13}CO than in the $C^{18}O$ emission lines. The LVG models suggest that the *Y*-component exhibits the lowest abundance ratio of all three components for $N(^{12}CO)/N(^{13}CO) \sim 30$ and the highest for $N(^{13}CO)/N(C^{18}O) \sim 1–3$, possibly suggesting a relatively high abundance for ^{13}CO. It is reasonably well constrained to have a warmer best-fit solution than the *X*- and *Z*-components ($T = 110–200$ K). The low abundance could be indicating that component *Y* is in a later stage of star formation, since ^{13}C are secondary nuclei produced in longer lived low-to-intermediate mass stars. In such a scenario this component may be the oldest of the three components. This is demonstrated by the different abundance ratio vectors in Fig. 4. We note that the *Y*-component SLED fits tend to overpredict the ^{13}CO and underpredict the $C^{18}O$ SLEDs and the best fit does not peak at a high enough excitation in $C^{18}O$.

Z-component – the *Z*-component is at the opposite edge of the gas disc from the *X*-component at a velocity of $\sim -70\,km\,s^{-1}$. It is very similar to the *X*-component in terms of *T*, $n(H_2)$ and abundance ratios. We observe it to be very weak in ^{13}CO but strong in $C^{18}O$, in particular the highest rotational energy, $C^{18}O(5–4)$. It also exhibits a high abundance ratio of $N(^{12}CO)/N(^{13}CO) \sim 100$ and a low abundance ratio of $N(^{13}CO)/N(C^{18}O) \sim 1$. The low $N(^{13}CO)/N(C^{18}O)$ ratio appears to be due to a genuinely high abundance of $C^{18}O$. A similarly high abundance is found in the *X*-component. We note that for the *Z*-component, the best-fit model peaks at $J_{up} \sim 4$ whereas the data peaks closer to $J_{up} = 5$ and the fit to the $C^{18}O(5–4)$ is underpredicted by $\sim 3\sigma$, so the temperature is potentially even higher. The properties of the *Z*-component are consistent with a warm, dense medium undergoing preferentially massive star formation.

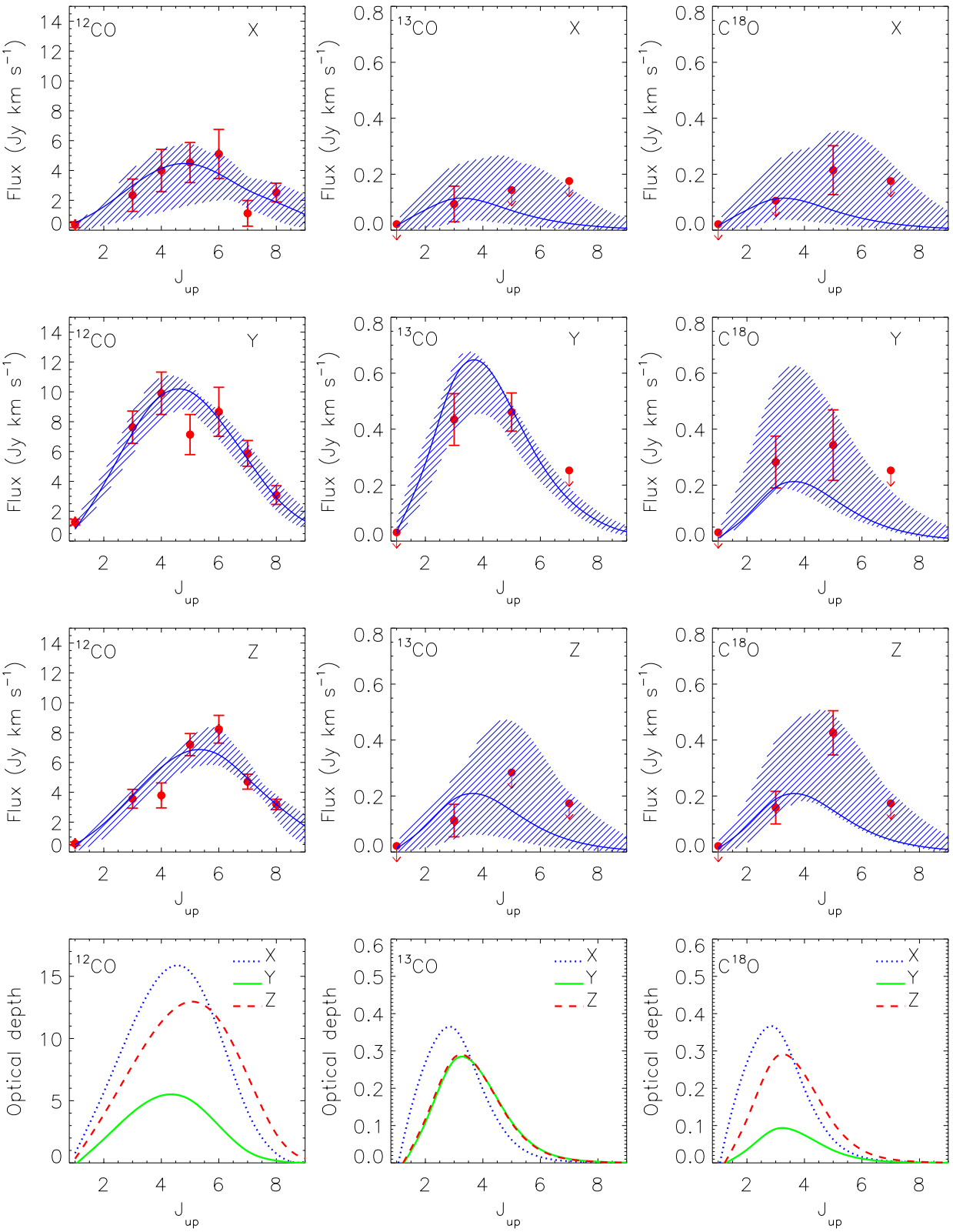

Figure 8. SLEDs for the individual kinematic components *X*, *Y* and *Z* in ^{12}CO, ^{13}CO and $C^{18}O$. Overlaid in hashed blue is the range in LVG model fits that are within $\Delta\chi^2 \leq 1\sigma$ of the best fit to the ^{13}CO, $C^{18}O$ and ^{12}CO data (all models that lie within $\Delta\chi^2 \leq 7.0$). The solid curve represents the model with the minimum total χ^2 value for the fit to all the SLEDs for that component. Upper limits are plotted at the 2σ level. The ^{13}CO and $C^{18}O$ SLEDs clearly peak at different J_{up} but this is not well described by the models. Bottom: the distribution of the optical depth values for the best-fit models to the individual components, demonstrating that the optical depth of ^{12}CO is ∼40 times higher than that of ^{13}CO and $C^{18}O$.

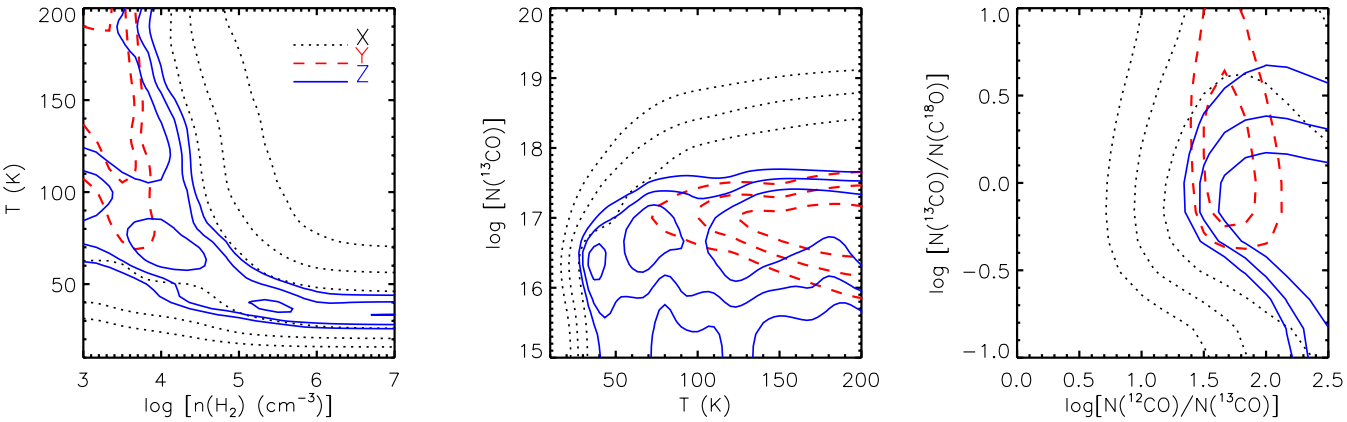

Figure 9. Parameter space distributions of the best-fit models in *X*, *Y* and *Z* components for different combinations of parameters. The contours represent the models lying within $\Delta\chi^2 = 1$, 2 and 3σ, which for six degrees of freedom corresponds to models within $\Delta\chi^2$ of 7.0, 12.8 and 20.0, respectively. These fits to the kinematically decomposed spectral line fluxes provide better constraints on the parameter space than those using the integrated emission. The different components are represented with different colours and line styles and it can be seen that the different components occupy different regions of parameter space, although there is overlap between all of them. The *X*-component is clearly the least constrained as we have fewer line detections in this component.

The similar *X*- and *Z*-components thus appear to be chemically younger than the *Y*-component and they may be similar structures.

The *X*- and *Z*-components require a lower abundance ratio of [^{13}CO]/[C^{18}O] than the *Y*-component and this abundance ratio is surprisingly low (<1), implying enhanced C^{18}O abundance in the outer regions of the galaxy. Whereas the *Y*-component exhibits the lowest ratio of $N(^{12}\mathrm{CO})/N(^{13}\mathrm{CO})$ out of the three components, potentially implying an enhanced ^{13}CO abundance in the dynamical centre of the galaxy.

5 DISCUSSION

Our measurements of optically thin ^{13}CO and C^{18}O in the ISM of SMM J2135 suggest a molecular gas mass of $M_{\rm gas} \sim (0.8{-}1.5) \times 10^{10}\,{\rm M}_{\odot}$ (see Section 4.4.1). When combined with the stellar mass, $M_* = (3.0 \pm 1) \times 10^{10}\,{\rm M}_{\odot}$, the implied dynamical mass ($M_{\rm dyn} = M_{\rm gas} + M_\star$) is within 2σ of that derived from the galaxy dynamics $M_{\rm dyn} = (6.0 \pm 0.5) \times 10^{10}\,{\rm M}_{\odot}$ (Swinbank et al. 2011), if we take the upper limit on our derived gas mass. We therefore derive a ratio of $M_{\rm gas}/M_{\rm dyn} \sim 0.25$ which is comparable to the average molecular gas fractions found for high-redshift star-forming galaxies of $M_{\rm gas}/M_{\rm dyn} \sim 0.3$–$0.5$ at $z \sim 1$–2 (Bothwell et al. 2013; Tacconi et al. 2013). Using $M_{\rm gas} \sim 1.5 \times 10^{10}\,{\rm M}_{\odot}$, we derive $\alpha_{\rm CO} \sim 0.9$ which is close to the canonical value for ULIRGs (i.e. Downes & Solomon 1998) but lower than our previous estimate of $\alpha_{\rm CO} = 2$ in Danielson et al. (2011).

Modelling the ^{12}CO, ^{13}CO and C^{18}O SLEDs, we find that the ISM is best described by a two-phase ISM comprising a 'cold' phase ($T_{\rm K} \sim 50$ K) tracing the extended gas disc, and a 'hot' phase ($T_{\rm K} \sim 90$ K), with an average density of $\sim 10^{3-4}$ cm^{-3} (presumably tracing the denser star-forming regions). However, due to the strong differences in $J_{\rm peak}$ for the ^{13}CO and C^{18}O SLEDs we find that a two-phase fit to the integrated emission is unable to adequately describe both simultaneously.

However, SMM J2135 exhibits highly structured molecular emission spectra, and previous work has demonstrated that the source can be kinematically decomposed into three main components which are coincident with the bright star-forming clumps visible in the high-resolution observed 870 μm SMA and JVLA ^{12}CO(1–0) maps (Swinbank et al. 2011). Thus, deriving the properties of such a complex system via the integrated flux, although illustrative for comparison to both local and high-redshift observational studies, is not probing the true conditions in the star-forming regions themselves. Furthermore, using optically thick gas tracers gives a biased view of the properties of the cold molecular gas and does not probe the densest regions in which the stars are forming. Thus, we fit a three-component kinematic model (*X*, *Y*, *Z*) to the spectra of the two lower abundance (and thus typically optically thinner) gas tracers: ^{13}CO and C^{18}O, in order to provide a more detailed understanding of the ISM conditions within this high-redshift star-forming galaxy. By kinematically decomposing the SLEDs into their constituent components (*X*, *Y* and *Z*) we show that there are no strong differences in the excitation of the ^{13}CO and C^{18}O in any of the components, although we do find abundance gradients between the components.

Danielson et al. (2011) proposed that the highly structured ^{12}CO emission line morphology of SMM J2135 arises from a merging system in which components *Y* and *Z* correspond to two different interacting galaxies with the *X*-component being a diffuse tidal feature. However, high-resolution (∼0.2 arcsec) dynamical maps of the ^{12}CO(6–5) and ^{12}CO(1–0) emission showed that the bulk of the gas in fact lies in a 5 kpc diameter, rotationally supported, clumpy disc (Swinbank et al. 2011). In this model, the highly structured ^{12}CO emission arises from a number of bright clumps within the disc.

Our new ^{13}CO and crucially, C^{18}O observations are consistent with the latter interpretation: the enhanced C^{18}O is found in the outer regions of the disc (the high C^{18}O is typically associated with young, high-mass star formation), and the enhanced ^{13}CO (generally associated with older, lower mass stars) is located in the central regions. However, we note that the gas disc has a very low Toomre *Q*, ($Q = 0.50 \pm 0.15$; Swinbank et al. 2011), suggesting that a significant, major accretion event must have recently occurred and the star formation has yet to stabilize the disc back to $Q = 1$ (e.g. Hopkins, Quataert & Murray 2012). One possible local analogue of SMM J2135 is the luminous galaxy NGC 6240 (e.g. Tacconi et al. 1999; Iono et al. 2007). This system has been found to comprise a thick, highly turbulent disk, centred between the two nuclei of the merging progenitors. In this system, the tidally stripped gas from the two progenitors has settled into a rotationally supported disc in the potential well of the remnant. The variations in abundance across SMM J2135 may imply that it is in a similar regime, since

such chemical variations and low Toomre Q are unlikely to arise through the gravitational collapse of a single disc.

5.1 Cosmic rays as a heating source

There is evidence that in some star-forming galaxies, heating from cosmic rays may play a more important role than photons, due to their ability to penetrate and volumetrically heat dense gas (e.g. Goldsmith & Langer 1978; Bradford et al. 2003; Hailey-Dunsheath et al. 2008; Bayet et al. 2011a,b; Papadopoulos et al. 2012a). Given the high SFR of this galaxy (SFR $\sim 400\,M_\odot\,yr^{-1}$), particularly in the clumps, we now look at the energetics of the heating and cooling of the cold dense gas in this system, comparing the potential contributions from cosmic ray and UV heating to the total cooling we expect from our CO lines (one of the main coolants in the cold ISM).

5.1.1 Cosmic ray heating rate

Following Suchkov, Allen & Heckman (1993) and Bradford et al. (2003), assuming that cosmic rays are produced at a rate proportional to the supernova rate, and hence the current SFR, and are removed from star-forming regions by high-velocity galactic winds, we derive the cosmic ray heating rate, χ_{H_2}, per H_2 molecule:

$$\chi_{H_2} = \zeta_p \Delta Q \ (\mathrm{erg\ s^{-1}\ per\ H_2}), \quad (9)$$

where, ζ_p is the ionization rate per H_2 molecule and ΔQ is the thermal energy deposited per ionization (17–20 eV; Goldsmith & Langer 1978). By scaling from the Milky Way we determine the ionization rate to be

$$\zeta_{p,SMMJ2135} = \zeta_{p,MW} \times \frac{\psi_{SMMJ2135}}{\psi_{MW}} \times \frac{v_{MW}}{v_{w,SMMJ2135}}, \quad (10)$$

where $\zeta_{p,\,MW}$ is the local Galactic ionization rate ($2–7 \times 10^{-17} s^{-1}$ for dense gas; e.g. Goldsmith & Langer 1978; van Dishoeck & Black 1986); $\psi_{SMMJ2135}$ is the supernova rate per unit area in SMM J2135; ψ_{MW} is the supernova rate per unit area (over the entire disc) of the Milky Way; v_w is the cosmic ray diffusion velocity from the Galactic disc and $v_{w,\,SMMJ2135}$ is the wind velocity of SMM J2135. We assume a Galactic SFR of 0.68–1.45 $M_\odot\,yr^{-1}$ across the whole disc (the upper limit taken from Robitaille & Whitney 2010), resulting in an SFR surface density of $\sum_{SFR,\,MW} = (9.6 - 20.1) \times 10^{-4}\,M_\odot\,yr^{-1}\,kpc^{-2}$ and we assume the cosmic ray diffusion velocity from the Galactic disc to be $v_w = 10\,km\,s^{-1}$ (Suchkov et al. 1993).

Previous observations have suggested that >50 per cent of the star formation in SMM J2135 may be occurring in the clumps, which appear to be closely associated with the kinematic components X, Y and Z (Swinbank et al. 2011). To search for cosmic ray heating, we therefore concentrate on these regions. We assume the supernova rate per unit area $\psi_{SMMJ2135}$ to be proportional to the SFR surface density in the clumps of SFR = 30–90 $M_\odot\,yr^{-1}$ (assuming a Salpeter IMF; Swinbank et al. 2011). We also assume clump radii of 100–200 pc, and that the stars do not migrate far from the clumps before they become supernovae. We adopt a wind velocity in SMM J2135 of $v_{w,\,SMMJ2135} = 200\,km\,s^{-1}$, approximately the FWHM of the individual components. Typical values for wind velocity in local starbursts and high-redshift submillimetre galaxies are $v_w = (1–3) \times 10^3\,km\,s^{-1}$ (Banerji et al. 2011) so $v_{w,\,SMMJ2135} = 200\,km\,s^{-1}$ is likely to be a lower limit (thus an upper limit on the cosmic ray heating rate). This suggests an ionization rate of $\zeta_{p,\,SMMJ2135} \sim (1–100) \times 10^{-13}\,s^{-1}$. Assuming $\Delta Q = 20$ eV per ionization, the power deposited per H_2 molecule is $\chi_{H_2} \sim (30–3300) \times 10^{-25}\,erg\,s^{-1}$. This is higher than the cosmic ray heating rate of $\chi_{H_2} = (5–18) \times 10^{-25}\,erg\,s^{-1}$ in the local starburst galaxy NGC 253 (Bradford et al. 2003). However, given that the average SFR is significantly higher in SMM J2135 than in NGC 253 (SFR $\sim$ 2–3 $M_\odot\,yr^{-1}$; Ott et al. 2005), it would be expected that the ionization rate from cosmic rays should be significantly higher.

Papadopoulos (2010) predicts high temperatures of >80–240 K in compact starbursts with cosmic ray ionization rates of $(5–20) \times 10^{-14}\,s^{-1}$. In SMM J2135, we derive a significantly higher ionization rate (up to 50 times higher) and furthermore, the best-fitting temperatures we derive using LVG modelling for the individual components X, Y and Z range between 140–200 K. Thus these high temperatures could also hint that the clumps may be dominated by cosmic ray heating.

5.1.2 UV heating rate

For comparison to the cosmic ray heating, we also estimate the likely UV photon heating per H_2 molecule from massive star formation assuming that the far-infrared luminosity is dominated by OB stars. The typical efficiency of photoelectric heating in PDRs is ~0.3 per cent (i.e. Weingartner, Draine & Barr 2006), therefore the UV heating input per H_2 molecule can be estimated using, $\chi_{H_2} = 0.003 L_{IR}/(M_{H_2}/m_{H_2})$. Given an intrinsic infrared luminosity (8–1000 μm) of $L_{IR} = 2.3 \times 10^{12}\,L_\odot$ (Ivison et al. 2010), we derive a heating rate per H_2 molecule of $\chi_{H_2} \sim 15 \times 10^{-25}\,erg\,s^{-1}$ over the whole system. Again, it is likely that the heating rate in the clumps is higher than the heating rate integrated over the whole system.

To estimate the UV heating per clump, we assume an average clump mass of $\sim 1.3 \times 10^9\,M_\odot$ (Danielson et al. 2011) and that each clump contributes ~1/8th of the observed L_{IR} ($\sim 3 \times 10^{11}\,L_\odot$), which is the typical clump fraction from the total 260 μm rest-frame emission (Swinbank et al. 2010). The heating rate per H_2 molecule can then be estimated to be $\chi_{H_2} \sim 45 \times 10^{-25}\,erg\,s^{-1}$. This is similar to the minimum heating per clump that could be provided by cosmic rays, hence we conclude that both UV and cosmic rays are energetically capable of heating the gas.

However, we can take this estimate one stage further and ask what is the necessary distribution of gas needed for PDRs to heat the whole reservoir of warm gas? If the warm gas in the system is being heated by PDRs, then all that gas has be to in the vicinity of a hot star to reach a far-UV radiation field of $G_0 \sim 1 \times 10^{3–3.6}$ Habing fields (Ivison et al. 2010; Danielson et al. 2011). Again, using the far-infrared luminosity of $2.3 \times 10^{12}\,L_\odot$ and making the approximation that the UV radiation field is dominated by O5 stars (luminosity $\sim 8 \times 10^5\,L_\odot$ per star), results in $\sim 3 \times 10^6$ O5 stars in SMM J2135. Using the SED of an O5 star, in order to have $G_0 \geq 1 \times 10^3$, the gas has to be within 3 pc of the star. So, using spheres of radius ~3 pc, assuming $\sim 3 \times 10^6$ O5 stars, and using the derived gas density, we can calculate the gas mass exposed to $G_0 \geq 1 \times 10^3$. For our minimum density of $n(H_2) \sim \times 10^3\,cm^{-3}$ (Section 4.4), this becomes $M \sim 1.6 \times 10^{10}\,M_\odot$ which is in reasonable agreement with our estimated gas mass from ^{13}CO (Section 4.4.1). However, the gas can only be heated by UV up to $A_V \sim 5$ mag from the star (e.g., Tielens & Hollenbach 1985, Fig. 7). For densities up to $2 \times 10^3\,cm^{-3}$, the whole ~3 pc radius sphere is in the $A_V < 5$ mag region. Thus, for gas densities between $(1–2) \times 10^3\,cm^{-3}$, the amount of PDR-heated gas will be between $M = (1.5–3.0) \times 10^{10}\,M_\odot$. If much of the gas is at significantly higher density then PDRs will not be able to provide enough heating, since only the surface layer is heated.

For example, for $n(H_2) \sim 1 \times 10^5\,cm^{-3}$, $A_V = 5$ is reached at only $\sim$0.3 pc from the star and the amount of gas that can be heated is only $M \sim 1.6 \times 10^8\,M_\odot$. Therefore, we can conclude that if the bulk gas density is significantly higher than $n(H_2) \sim 2 \times 10^3\,cm^{-3}$ (which indeed we may be observing in some of the star-forming regions), then PDRs will not be able to provide the heating, and we need a mechanism that is capable of volumetrically heating the gas, such as cosmic rays.

5.1.3 Cooling rate

To estimate the cooling rate per H_2 molecule, we calculate the total CO luminosity in all species following Solomon & Vanden Bout (2005) and Hailey-Dunsheath et al. (2008):

$$\Sigma L_{CO} = \Sigma 1.04 \times 10^{-3} S_{CO,i} \Delta V \nu_{rest,i} D_L^2 (1+z)^{-1}/\mu, \quad (11)$$

where μ is the magnification factor of 37.5 ± 4.5 and D_L is the luminosity distance in Mpc. We estimate a total intrinsic CO luminosity of $L_{CO} \approx 1.8 \times 10^8\,L_\odot$. Using our cold gas mass estimated from ^{13}CO(3–2) of $M_{gas} = 1.5 \times 10^{10}\,M_\odot$, our cooling rate per H_2 molecule is $L_{CO}/(M_{H_2}/m_{H_2}) \sim 0.8 \times 10^{-25}\,erg\,s^{-1}$. In this calculation, we have not included the [C II] 157.8 μm emission which is the dominant coolant in the outer envelopes of molecular clouds. Including the [C II] 157.8 μm in our calculation our cooling per H_2 becomes $\chi_{H_2} \sim 20 \times 10^{-25}\,erg\,s^{-1}$. However, at high A_V ($A_V > 5$) the [C II] 157.8 μm abundance significantly decreases and so has a minimal contribution to the cooling in these regions.

5.1.4 Balancing the temperature

We have derived heating rates from cosmic rays and UV photons of $(30–3300) \times 10^{-25}\,erg\,s^{-1}$ and $\sim 45 \times 10^{-25}\,erg\,s^{-1}$, respectively, and we derive cooling rates from the atomic and molecular line emission of $\sim(0.8–20) \times 10^{-25}\,erg\,s^{-1}$. Although crude, overall this shows that both the cosmic ray and UV heating rates are comparable to the cooling rate. However, we also demonstrate that for densities of $n(H_2) > \times 10^5\,cm^{-3}$, UV heating (from O5 stars) would not provide enough heating, due to extinction.

Moreover, Papadopoulos et al. (2012a) have suggested that in regions of enhanced cosmic ray density, the cosmic rays are able to penetrate to the core of the dense gas and volumetrically raise the temperature of the star-forming cores, which sets new initial conditions for star formation and increases the characteristic mass of young stars.

Therefore, although we estimate that both the UV and cosmic rays are capable of balancing the cooling rate in SMM J2135, the high gas densities and the high (>100 K) temperatures we derive for the star-forming clumps may provide indirect evidence that cosmic ray heating is particularly important in the individual kinematic components of SMM J2135. It is therefore possible that we are seeing evidence of this where we see an enhancement of $C^{18}O$, which is also indicative of preferentially massive star formation, possibly due to a raised initial temperature for star formation in these regions.

Finally, it is important to note that as well as cosmic ray heating and photon heating discussed here, X-ray heating, shocks and turbulent heating have been found to play an important role in the heating of interstellar gas both in the Milky Way and in other systems. Swinbank et al. (2011) finds a highly turbulent ISM in SMM J2135 and turbulence can have a similar effect to cosmic rays of volumetrically heating the gas (i.e. Meijerink et al. 2011, 2013; Papadopoulos et al. 2012a; Ao et al. 2013).

6 CONCLUSIONS

We analyse observations of ^{13}CO and $C^{18}O$ emission from the lensed, $z = 2.3$ ULIRG, SMM J2135. We have combined these observations with our previous ^{12}CO measurements to better constrain the conditions in the ISM of this system by analysing the galaxy-integrated fluxes and the kinematically decomposed emission. Using these lower abundance tracers of H_2 we have been able to remove some of the degeneracies in modelling the ISM. We summarize our conclusions as the following.

(i) We demonstrate that the ^{13}CO emission is likely to be optically thin ($\tau \ll 1$) and we use this to estimate the total cold gas mass of $M_{gas} \sim 1.5 \times 10^{10}\,M_\odot$ which is consistent with the dynamical and stellar limits on the total mass of the system. This implies $\alpha_{CO} \sim 0.9$ for this high-redshift ULIRG.

(ii) We detect $C^{18}O$ and measure a surprisingly high flux resulting in a $^{13}CO/C^{18}O$ flux ratio $\sim$4–15 times lower than that measured in the Milky Way. Since ^{18}O is associated with the winds from massive stars, it is possible that this enrichment of $C^{18}O$ may be due to the presence of preferentially massive star formation.

(iii) The ISM is best described by a two-phase model; a 'cold' phase at $\sim$50 K with a density of $n(H_2) \sim 10^3\,cm^{-3}$, and a 'hot' phase at $\sim$90 K and $n(H_2) \sim 10^4\,cm^{-3}$, respectively. However, the SLEDs of ^{13}CO and $C^{18}O$ peak at different J_{up} despite both appearing to be optically thin. We attribute this to variations of $[^{13}CO]/[C^{18}O]$ within the galaxy and therefore kinematically decompose the line emission from the system into three main components, *X*, *Y* and *Z*. We find that the *Y*-component, which appears to be coincident with the centre of mass of the system, is warm ($T_K \sim 140$ K) and dense ($n(H_2) \sim 10^{3.5}\,cm^{-3}$) potentially with a higher abundance of ^{13}CO ($[^{12}CO]/[^{13}CO] \sim 30$) implying older star formation from intermediate mass stars. In contrast, the *Z*- and *X*-components are similar to each other. Both these regions display low $[^{13}CO]/[C^{18}O]$ ratios possibly implying enhanced massive star formation leading to a higher abundance of $C^{18}O$ in these regions.

(iv) We have derived an average cooling rate from all the observed CO lines of $\sim(0.8-20) \times 10^{-25} erg\,s^{-1}$ per H_2 molecule. We determine the possible contribution to the heating from cosmic rays (originating largely in supernovae) and from UV photon heating of $(30–3300) \times 10^{-25}\,erg\,s^{-1}$ and $\sim 45 \times 10^{-25}\,erg\,s^{-1}$, respectively. Although crude, both cosmic ray heating and UV heating can plausibly balance the cooling occurring in the system. However, the high temperatures ($T_K = 140-200$ K) derived in the highest density components may suggest that cosmic rays may play a more important role than UV heating in this system.

Since SMM J2135 is a representative high-redshift ULIRG, this study paves the way for future detailed studies of this population. With Atacama Large Millimetre Array (ALMA) in full science operations we will be able to resolve sub-kpc structure in these faint lines and derive resolved ISM properties. Furthermore, ALMA will enable the important observations of high-density chemical tracers such as CS and HCN, giving insight into the origin of the intense star formation activity in this galaxy and potentially testing for systematic variation in the relative abundances of ^{12}CO, ^{13}CO and $C^{18}O$ which may reflect variation in the IMF.

ACKNOWLEDGEMENTS

We would like to thank the anonymous referee for a thorough and constructive report which significantly improved the content and clarity of this paper. ALRD acknowledges an STFC studentship

(ST/F007299/1). AMS gratefully acknowledges an STFC Advanced Fellowship through grant ST/H005234/1. IRS acknowledges support from STFC, a Leverhulme Fellowship, the ERC Advanced Investigator programme DUSTYGAL 321334 and a Royal Society/Wolfson Merit Award. We thank Francoise Combes and Steve Hailey-Dunsheath for useful conversations and Padelis Papadopoulos for extensive comments and useful suggestions. We thank John Helly for his help. We thank the IRAM staff Melanie Krips and Roberto Neri for help provided during the observations and for data reduction guidance. The research leading to these results has received funding from the European Commission Seventh Framework Programme (FP/2007-2013) under grant agreement No 283393 (RadioNet3). The raw data from JVLA and IRAM on which this analysis is based can be accessed through the JVLA archive (programme code 11B-062) and through contacting IRAM with the programme code U0B6.

REFERENCES

Aalto S., Booth R. S., Black J. H., Johansson L. E. B., 1995, A&A, 300, 369
Ao Y., Henkel C., Menten K. M., Requena-Torres M. A., Stanke T., Mauersberger R., Aalto S., Mühle S., 2013, A&A, 550, A135
Bally J., Langer W. D., 1982, ApJ, 255, 143
Banerji M., Chapman S. C., Smail I., Alaghband-Zadeh S., Swinbank A. M., Dunlop J. S., Ivison R. J., Blain A. W., 2011, MNRAS, 418, 1071
Bayet E., Williams D. A., Hartquist T. W., Viti S., 2011a, MNRAS, 414, 1583
Bayet E., Viti S., Hartquist T. W., Williams D. A., 2011b, MNRAS, 417, 627
Bayet E. et al., 2013, MNRAS, 432, 1742
Bergin E. A., Tafalla M., 2007, ARA&A, 45, 339
Bothwell M. S. et al. 2013, MNRAS, 429, 3047
Bradford C. M., Nikola T., Stacey G. J., Bolatto A. D., Jackson J. M., Savage M. L., Davidson J. A., Higdon S. J., 2003, ApJ, 586, 891
Bryant P. M., Scoville N. Z., 1996, ApJ, 457, 678
Casoli F., Dupraz C., Combes F., 1992a, A&A, 264, 49
Casoli F., Dupraz C., Combes F., 1992b, A&A, 264, 55
Danielson A. L. R. et al., 2011, MNRAS, 410, 1687
Dickman R. L., Snell R. L., Schloerb F. P., 1986, ApJ, 309, 326
Downes D., Solomon P. M., 1998, ApJ, 507, 615
Flower D. R., 2001, MNRAS, 328, 147
Frerking M. A., Langer W. D., Wilson R. W., 1982, ApJ, 262, 590
Gao Y., Solomon P. M., 2004, ApJ, 606, 271
Genzel R. et al., 2012, ApJ, 746, 69
Goldreich P., Kwan J., 1974, ApJ, 189, 441
Goldsmith P. F., Langer W. D., 1978, ApJ, 222, 881
Greve T. R., Papadopoulos P. P., Gao Y., Radford S. J. E., 2009, ApJ, 692, 1432
Hailey-Dunsheath S., Nikola T., Stacey G. J., Oberst T. E., Parshley S. C., Bradford C. M., Ade P. A. R., Tucker C. E., 2008, ApJ, 689, L109
Harrison A., Henkel C., Russell A., 1999, MNRAS, 303, 157
Henkel C., Mauersberger R., 1993, A&A, 274, 730
Henkel C., Mauersberger R., Wiklind T., Huettemeister S., Lemme C., Millar T. J., 1993, A&A, 268, L17
Henkel C., Chin Y.-N., Mauersberger R., Whiteoak J. B., 1998, A&A, 329, 443
Henkel C., Downes D., Weiß A., Riechers D., Walter F., 2010, A&A, 516, A111
Hopkins P. F., Quataert E., Murray N., 2012, MNRAS, 421, 3488
Iono D. et al., 2007, ApJ, 659, 283
Ivison R. J. et al., 2010, A&A, 518, L35
Martín S., Aladro R., Martín-Pintado J., Mauersberger R., 2010, A&A, 522, A62
Matsushita S. et al., 2009, ApJ, 693, 56
Meier D. S., Turner J. L., 2001, ApJ, 551, 687
Meier D. S., Turner J. L., 2004, AJ, 127, 2069
Meijerink R., Spaans M., Loenen A. F., van der Werf P. P., 2011, A&A, 525, A119
Meijerink R. et al., 2013, ApJ, 762, L16
Ott J., Weiss A., Henkel C., Walter F., 2005, ApJ, 629, 767
Papadopoulos P. P., 2010, ApJ, 720, 226
Papadopoulos P. P., Seaquist E. R., Scoville N. Z., 1996, ApJ, 465, 173
Papadopoulos P. P., van der Werf P. P., Xilouris E. M., Isaak K. G., Gao Y., Mühle S., 2012a, MNRAS, 426, 2601
Papadopoulos P. P., van der Werf P., Xilouris E., Isaak K. G., Gao Y., 2012b, ApJ, 751, 10
Penzias A. A., 1983, ApJ, 273, 195
Petitpas G. R., Wilson C. D., 2000, ApJ, 538, L117
Prantzos N., Aubert O., Audouze J., 1996, A&A, 309, 760
Robitaille T. P., Whitney B. A., 2010, ApJ, 710, L11
Scoville N. Z., Sargent A. I., Sanders D. B., Claussen M. J., Masson C. R., Lo K. Y., Phillips T. G., 1986, ApJ, 303, 416
Solomon P. M., Vanden Bout P. A., 2005, ARA&A, 43, 677
Solomon P. M., Downes D., Radford S. J. E., Barrett J. W., 1997, ApJ, 478, 144
Spergel D. N. et al., 2003, ApJS, 148, 175
Spergel D. N. et al., 2007, ApJS, 170, 377
Stark D. P., Swinbank A. M., Ellis R. S., Dye S., Smail I. R., Richard J., 2008, Nat, 455, 775
Stott J. P. et al., 2013, MNRAS, preprint (arXiv:1309.0506)
Suchkov A., Allen R. J., Heckman T. M., 1993, ApJ, 413, 542
Swinbank A. M. et al., 2010, Nat, 464, 733
Swinbank A. M. et al., 2011, ApJ, 742, 11
Tacconi L. J., Genzel R., Tecza M., Gallimore J. F., Downes D., Scoville N. Z., 1999, ApJ, 524, 732
Tacconi L. J. et al., 2013, ApJ, 768, 74
Tan Q.-H., Gao Y., Zhang Z.-Y., Xia X.-Y., 2011, Res. Astron. Astrophys., 11, 787
Tielens A. G. G. M., Hollenbach D., 1985, ApJ, 291, 722
van der Tak F. F. S., Black J. H., Schöier F. L., Jansen D. J., van Dishoeck E. F., 2007, A&A, 468, 627
van Dishoeck E. F., Black J. H., 1986, ApJS, 62, 109
Wang M., Henkel C., Chin Y.-N., Whiteoak J. B., Hunt Cunningham M., Mauersberger R., Muders D., 2004, A&A, 422, 883
Watson W. D., Anicich V. G., Huntress W. T., Jr, 1976, ApJ, 205, L165
Weingartner J. C., Draine B. T., Barr D. K., 2006, ApJ, 645, 1188
Weiß A., Downes D., Walter F., Henkel C., 2005, A&A, 440, L45
Wilson T. L., Rood R., 1994, ARA&A, 32, 191
Wouterloot J. G. A., Brand J., 1996, A&AS, 119, 439
Young J. S., Scoville N. Z., 1991, ARA&A, 29, 581
Zhu L.-B., Yang J., Wang M., 2007, Chin. Astron. Astrophys., 31, 387

This paper has been typeset from a TEX/LATEX file prepared by the author.